UCLouvain

École polytechnique de Louvain

3D and 4D characterization of vascular tissue: opportunities and challenges

Author: **Maïté Pétré**
Supervisors: **Greet Kerckhofs, Valérie Lacroix**
Readers: **Thomas Pardoen, Nele Famaey**
Academic year 2019–2020
Master [120] in Chemical and Materials Engineering

Acknowledgments

First of all, I would like to express my sincere gratitude to my supervisor Prof. Dr. Greet Kerckhofs for her support during this entire year, a bit extended due to the covid-19. Although being a very busy person, she always found the time to discuss with me about my progress and the crazy organization needed to perform my experiments. I would like to thank her for her constructive and regular feedbacks, and her availability. My gratitude goes also to Prof. Dr. Valérie Lacroix for being at the initiative of this thesis topic.

I would like to express my gratitude to the FIBEr lab team, Prof. Dr. Nele Famay, Dr. Heleen Fehevary, Kimeberly Crevits and Klaas Vander Linden for their expertise on the planar biaxial testing machine and allowing me to perfom my experiments in their lab. My gratitude goes, especially, to Heleen for the time she spent training me, for her countless advises and her help in the data processing. In addition, I would like to acknowledge Lisa Leyssens, Camille Pestiaux, Sarah Vangrunderbeeck and Dr. Delia Hoffmann for their expertise on the CE-CT and for their help in preparing with me my experiments.

I would like to thank my parents, my sisters and Nicolas for their countless encouragements throughout my studies and especially during this Master's thesis.

Finally, I would like to give a special thanks to Charline and Aurélie and all my friends with whom I collaborated throughout the past five years. Their advice and external view were helpful and inspiring to solve problems. Thank you for all the great moments we shared and all the laughters we had.

Abstract

Cardiovascular diseases (CVDs) are the leading cause of death globally. In order to design better treatments, it is necessary to fully characterize the mechanical behavior of arteries and its relationship with their microstructure. This could be achieved by a novel imaging method, where in situ mechanical testing is combined with contrast-enhanced 3D microfocus X-ray computed tomography (CE-CT); further referred to as 4D CE-CT. The challenge of 4D CE-CT is the need of a constrast enhancing staining agent (CESA) to visualize arteries with good contrast. Indeed, the CESA used should not affect the mechanical properties of arteries.

The aim of this master thesis was two-fold. First, an image analysis protocol has been defined in order to fully characterize the microstructure of arteries using CE-CT, such as the inner and outer diameter, the luminal surface and the wall thickness. Moreover, with an appropriate threshold, the elastin lamellae in the media layer have been segmented from the rest of the aorta, and the number of lamellae, their thickness and structure separation have been computed. All results have been compared with values found in the literature.

Second, the effect of the CESA staining, of the staining time and of a preservation solution on the mechanical properties of arteries have been characterized. Different samples have been tested under planar biaxial mode. One concluded that sample aging had no effect on the mechanical properties of arteries. However, the staining by the CESA led to a stiffening effect of 20 to 30 kPa for a 15% strain. The staining time had no influences, and no clear conclusion on the effect of the preservation solution could be made.

As a conclusion, this study emphasised the challenges of obtaining sufficient contrast for CE-CT imaging and image analysis of the samples without influencing the mechanical properties of arteries. Further perspectives would be to test fresh samples (i.e. non-frozen samples) and to have more samples per condition to confirm and strengthen our findings.

Contents

List of Abbreviations and Symbols

Symbol	Description	Unit
CVDs	Cardiovascular diseases	
PAOD	Pheripheral artery occlusive disease	
CE-CT	Contrast enhancing micro-CT	
CESA	Contrast enhancing staining agent	
Hf-WD POM	Hafnium-substituted Wells-Dawson polyoxometalate	
Mono-WD POM	Monolacunary Wells-Dawson polyoxometalate	
ROI	Region of interest	
PBS	Phosphate-buffered saline solution	
σ	Cauchy stress	MPa
σ_{11}	Cauchy stress in the circumferential direction	MPa
σ_{22}	Cauchy stress in the axial direction	MPa
P	First Piola Kirchhoff stress	MPa
RF_{ij}	Reaction force in the i-th direction acting on an area with normal in the j-th direction	N
$A_{0,j}$	Undeformed area with normal in the j-th direction	mm^2
J	Jacobian calculated as the determinant of the deformation gradient	
F	Deformation gradient	
GOH	Gasser-Odgen-Holzhapfel material model	
C_{10}	Material parameter of the Gasser-Ogden-Holzapfel model	MPa
k_1	Material parameter of the Gasser-Ogden-Holzapfel model	MPa
k_2	Dimensionless material parameter of the Gasser-Ogden-Holzapfel model	
κ	Structural parameter of the Gasser-Ogden-Holzapfel model	
α	Structural parameter of the Gasser-Ogden-Holzapfel model	rad
E_{11}	Stiffness in the circumferential direction	MPa
E_{22}	Stiffness in the axial direction	MPa
NRMSE	Normalized root mean square error	

List of Figures

List of Tables

1

Introduction

Cardiovascular diseases (CVDs) are the number one cause of death globally. Every year around 18 million people die from CVDs, which represent 31% of all deaths worldwilde according to the World Health Organization [17]. This number continues to rise due to the persistence of cigarette smoking, unhealthy diet and obesity and the continuously aging population. If some of these risks factors can be reduced by a change of lifestyle, often it remains insufficient.

Among CVDs, the pheripheral artery occlusive disease (PAOD) affects a large number of the population and requires often a specific surgical intervention. It is estimated that over 200 million people are diagnosed with PAOD worldwide [18]. PAOD is characterized by narrowing so called stenosis, and occlusion of large and medium-sized arteries. If the obstruction is detected early enough, the blood clot or plaque can be removed by thrombolysis therapy where a catheter is used to dissolve and thus remove the clot or the plaque. However, after long time obstruction arteries tend to calcify and infrainguinal arterial bypass surgery must be performed. Infrainguinal arterial bypass surgery consists in replacing the calcified, diseased artery segment by an autologous vessel or a prosthetic graft. Autologuous vessels are preferred, but are often not available due to previous surgery or because of their poor quality [19]. Unfortunately, replacement of arteries with purely synthetic polymeric conduits often leads to the failure of such grafts. The main reason for this is the lack of knowledge on the mechanical and structural properties of arteries, which prevents good resemblance between synthetic grafts and arteries. Indeed, arteries posses a complex heterogeneous structure that imparts unique mechanical properties, which up to now remain difficult to mimic in arterial synthetic grafts .

The first step towards a deeper understanding and an improved design for synthetic grafts is to analyze the mechanical properties of arteries and characterize their micro-structure. For the first, mechanical tests, such as planar biaxial and uniaxial testing, can be used. Uniaxial tests are used to determine failure properties of a material and provide an ultimate tensile stress/strain value. Biaxial testing provides anisotropic compliance properties and mimics the physiological loading of soft tissues, such as vascular tisssues. For the structural characterization, non-destructive imaging techniques such as 3D microfocus X-ray computed tomography (micro-CT) can be used. 3D micro-CT enables visualizing the 3D morphology of hard tissues. It relies on differences in absorption of X-rays through the material. However, because soft tissues posses similar density and low atomic number, micro-CT alone is not sufficient to visualize their 3D structure with high contrast. Therefore, contrast enhancing staining agents (CESAs) can be used to improve contrast. This give rise to 3D contrast-enhanced micro-CT (CE-CT).

Nonetheless, if one could combine 3D CE-CT and the mechanical testing in one, we could obtain the arterial mechanical properties in situ. This would give rise to 4D CE-CT characterization, where structural and mechanical properties of arteries would be assessed in real time mimicking their *in-vivo* state characterized by a perpetual physiological loading. A major concern of 4D CE-CT is the CESA used to visualize soft tissues. Indeed those should not affect the mechanical properties of vascular tissues.

The goals of this master thesis are, therefore, (i) to characterize the mechanical and structural properties of arteries, and (ii) to investigate the influence of a CESA on the mechanical properties of vascular tissues.

2

State-of-the-art

2.1 Arteries

Blood is carried through the body via blood vessels. An artery is a blood vessel that carries blood away from the heart, where it branches into smaller vessels, named arterioles. Arterioles further branch into tiny capillaries, where nutrient and waste exchanges take place. Then, blood exits the capillaries via venules, small blood vessels that carry blood to a vein. The vein, being a larger blood vessel, returns the blood to the heart.

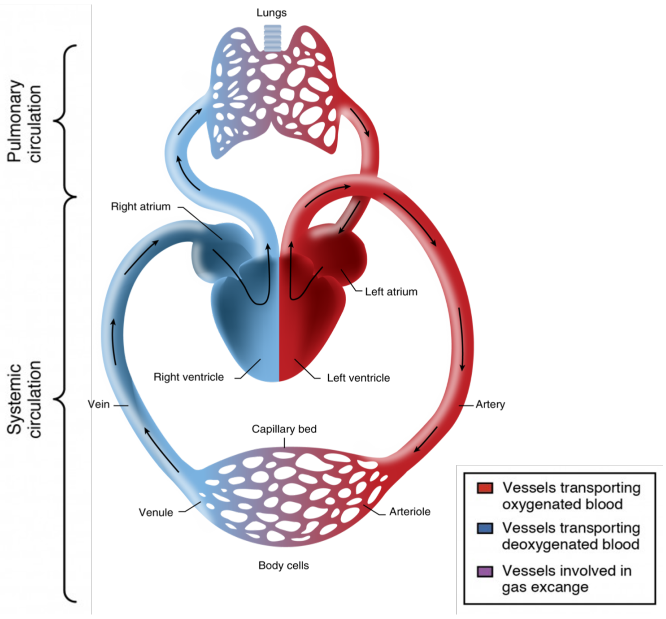

Figure 2.1: *The pulmonary circulation moves blood from the right side of the heart to the lungs for blood re-oxygenation and back to the heart. The systemic circulation moves blood rich in oxygen from the left side of the heart to the body and returns low oxygenated blood to the right side of the heart to repeat the cycle. The arrows indicate the direction of blood flow, and the colors show the relative levels of oxygen concentration. Adapted from [1, 2].*

Arteries and veins transport blood into two distinct circuits: the systemic and the pulmonary circuit. Systemic arteries provide oxygen-rich blood to the tissues in the body. The blood low in oxygen is carried by systemic veins and returns to the heart. In contrast, in the pulmonary circuit, pulmonary arteries carry blood low in oxygen exclusively to the lungs for gas exchange, and the pulmonary veins return the freshly oxygenated blood from the lungs to the heart to be pumped back out into the systemic circulation (Figure 2.1).

Although arteries and veins share certain features, they differ structurally and functionally. Arteries have thicker walls than veins because they are closer to the heart and receive blood at a far greater pressure. Arteries posses a more complex heterogeneous structure that imparts unique mechanical properties, which up to now remain difficult to characterize (Figure 2.2). These properties are non-linearity, anisotropy, viscoelasticity and compliance. To better understand these mechanical properties, a description of the anatomy and structural characteristics of arteries are essential.

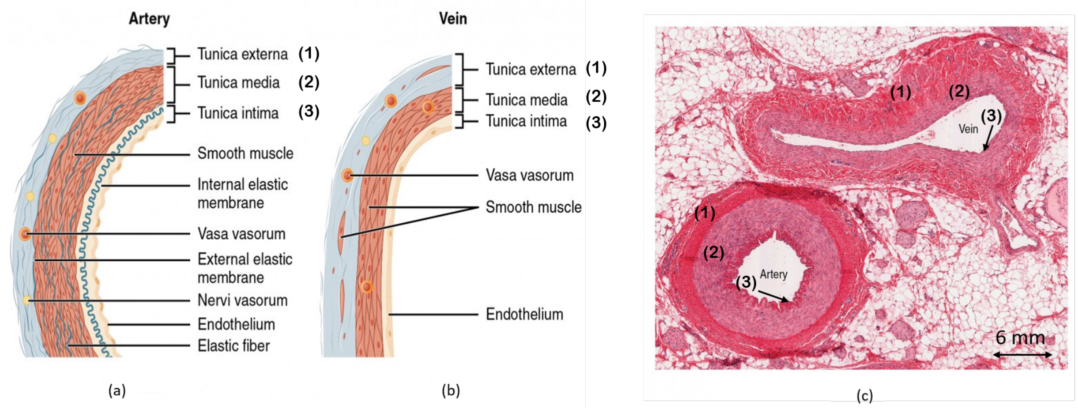

Figure 2.2: *(a) Arteries and (b) veins share certain general features such as the three same layer, but the walls of arteries are much thicker because of the higher pressure of the blood that flows through them. (c) A histological section (H&E stained) shows the relative difference in thickness. Adapted from [1].*

2.1.1 Anatomy and microstructure

An arterial wall is composed of three distinct layers including intima, media and adventitia, respectively (Figure 2.3). The layers consist of common components such as collagen, elastin and smooth muscle cells.

- The adventitia (outermost layer of an artery) typically consists mainly of dense collagen fibers, elastin fibers, and some fibroblasts and fibrocytes organized in thick bundles and serves to protect the vessel wall from over-stretch [20]. The collagen and elastin fibers are oriented in the direction along the vessel axis.

- The media layer which mainly defines the mechanical behaviour of the artery, is the thickest one. It is composed of circumferentially and coherently aligned elastin fibers, smooth muscle cells and collagen fibers. This structured arrangement gives the media an ability to resist high loads in the circumferential direction. The contraction and relaxation of the smooth muscle cells decrease and increase the diameter of the vessel lumen, respectively. Vasoconstriction decreases the blood flow as the smooth muscle in the walls contracts, making the vessel lumen narrower and increasing the blood pressure. Similarly, vasodilation increases the blood flow as smooth muscle relaxes, allowing the lumen to widen and the blood pressure to drop. Both vasoconstriction and vasodilation are regulated in part by small vascular nerves that run within the walls of blood vessels [1, 21].

- The intima (innermost layer of an artery) consists of endothelial cells and a few collagen fibers resting on a thin basal lamina. The intima is in direct contact with the blood flow. For young and healthy adults, the intima does not contribute to the overall mechanical behavior of the vessel wall. However, with age and diseases such as atherosclerosis the intima thickens and stiffens [22].

In general, arteries can be distinguished into two types: elastic arteries and muscular arteries (Figure 2.3). Elastic arteries are large-diameter vessels located more proximally (i.e. closer to the heart), such as the aorta and the pulmonary artery. They posses a much thicker media compared to muscular arteries, this allows the walls to stretch to accommodate the blood surge, when the heart contracts, and ejects blood into these arteries. Muscular arteries have a smaller diameter and are located more distally (i.e. closer to the arterioles), such as the femoral and coronary arteries. These arteries distribute blood to various parts of the body and their walls are constitued of a lot of smooth muscle cells. This enables them to contract or relax (dilate) to change the amount of blood delivered, as needed [23]. Moreover, several arteries exhibit also morphological structures of both types [21].

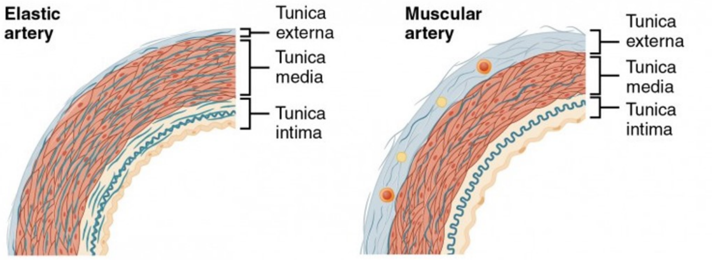

Figure 2.3: *Comparison of the walls of an elastic artery and a muscular artery. The arterial wall consists of three layers: the intima, the media and the externa, also called adventitia. Adapted from [1].*

The main systemic artery of the vascular system is the aorta, which consists of different segments: the ascending aorta, the arch, the descending thoracic aorta and the abdominal aorta (Figure 2.4). For a healthy subject, the mean inner diameter and wall thickness of the aorta is about 2.1 cm and 3 mm, respectively. However, the size of the aorta increases upon aging with a normal expansion rate of about 1-2mm/year. The aging of the aorta is accompanied by a loss of compliance and an increase in wall stiffness caused by structural changes including an increase in the collagen content and in calcification. Moreover, the microstructure and hence the mechanical behavior of a healthy arterial wall varies with the species, age, location along the vascular tree and disease [24].

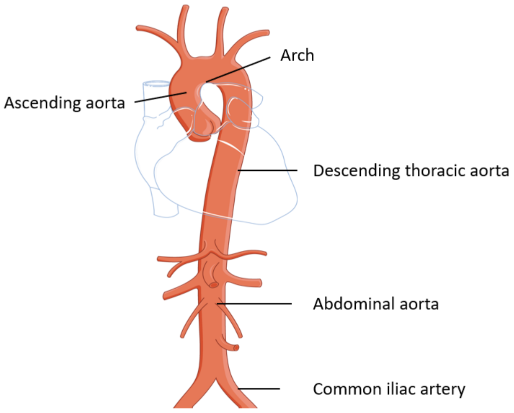

Figure 2.4: *The aorta with its main segments. Adapted from [3].*

2.1.2 Mechanical properties

Blood vessels, due to their unique structural composition impart complex mechanical properties such as anisotropy, non-linearity, compliance and viscoelasticity. Their mechanical behavior is based on their main structural components, i.e. elastin and collagen, which differ significantly in their elastic modulus (elastin = 0.6–1 MPa, collagen = 1 GPa) and in their waviness configuration [4]. In the following, the focus will be on the stress response of blood vessels, their compliance and their viscoelasticity, and fatigue properties.

2.1.2.1 Stress response

The stress response of an artery changes upon the load applied and can be divided in three distinct regions. The first region corresponds to the initial slope of the stress-strain curve of an artery and is contributed entirely by the elastin fibers. It is represented by a more or less linear slope. As load increases, successive transition of load from elastin to collagen occurs. This transition region II corresponds to the normal *in-vivo* operating range of pressure (80–120 mmHg) of an artery. In region III, the mechanical response is only dictated by collagen fibres. This incremental increase in elastic modulus is called the non-linearity property and is easily understood by looking at the random and wavy configuration of the elastin and collagen fibers in Figure 2.5. Indeed, due to the different orientation and waviness configuration of elastin and collagen fibers, they will not react at the same physiological pressure. Elastin fibers will be the first to straighten at low physiological pressure 80 mmHg (region I), while collagen fibers will straighten at higher values of physiological pressure. A further increase in pressure results in stretching of elastin and successive straightening, as well as stretching, of collagen fibers until the end of the physiological range (120 mmHg) is reached, corresponding to the end of region II. If one goes beyond this physiological range, collagen fibers will be fully stretched and the arterial behavior will be dominated by the stress response of the collagen fibers only, which is represented in region III.

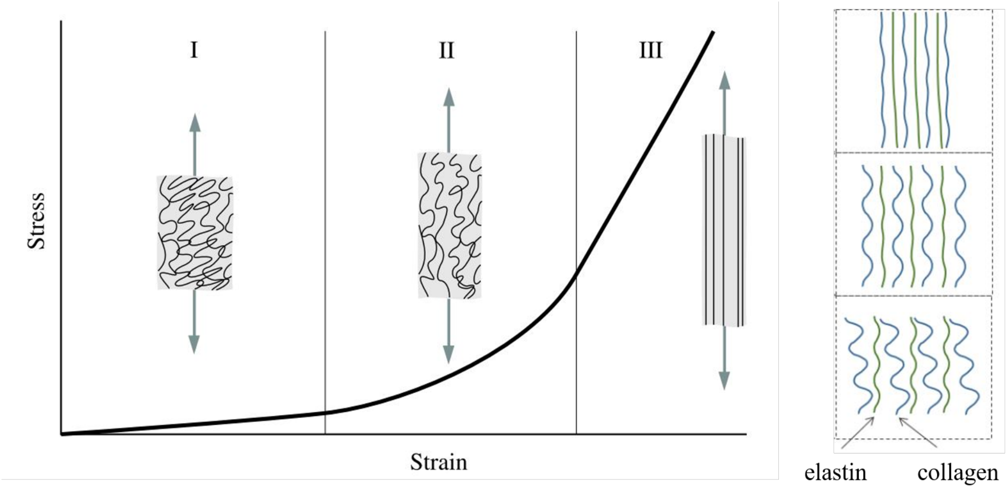

Figure 2.5: *The stress-strain curve of arteries can be divided in three parts. Adapted from [4, 5].*

Moreover, the mechanical behavior of arteries is also controlled by the relative proportion of collagen and elastin fibers, which tends to significantly differ from one artery to another. In the ascending aorta, for example, the elastin content is about 41% of dry weight while the descending aorta presents only 30% of elastin content [4].

2.1.2.2 Compliance

Arterial compliance is defined as the radial extensibility of an artery in the physiological pressure range (80-120 mmHg), and is measured in ml/mmHg. It is a crucial property as arteries need to adapt their diameter to maintain a relative continuous flow rather than a pulsatile flow, which would be much more energetically costly for the cardiovascular system. Indeed, arteries, by being distensible, act as elastic reservoir and modify the enormous fluctuation in blood pressure generated during the systolic and diastolic phases of cardiac contraction to a fairly uniform pressure, allowing a continuous flow of blood through the remaining circulation. Compliance provides, thus, a pulse-reducing effect on the flow of blood throughout the system by passive expansion and elastic recoil, allowing to maintain a relative constant artery wall shear stress [25, 26]. This is also known as the Windkessel function. This property is even more essential for arteries in the proximity of the heart such as the ascending aorta whose cross-sectional area can increase up to 11% [4].

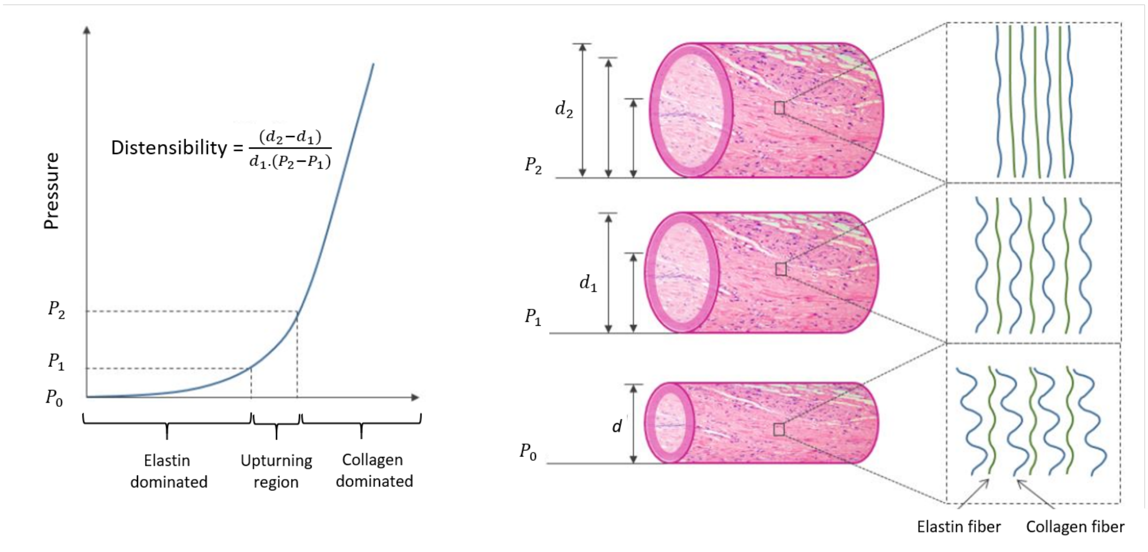

Figure 2.6: *Influence of elastin and collagen on the pressure-diameter relation of an artery. On the left, the graph shows the relation between the pressure of the blood flow and the variation that it provokes in the diameter, information needed to compute the distensibility with the depicted formula. On the right, the collagen (blue) and elastin (green) fibres under different levels of pressure can be observed [4, 6]. Adapted from [4].*

Figure 2.6 represents the same graph as in Figure 2.5, but here the stress and strain are expressed in function of the pressure and the diameter change. This allows to have a direct insight of the notion of distensibility and thus compliance. Indeed, distensibility is defined as the relative change in diameter for a given pressure change in the upturning region, whereas compliance is defined as the absolute change in diameter for a given pressure step :

$$distensibility = \frac{(d_2 - d_1)}{d_1 \times (P_2 - P_1)} \tag{2.1}$$

$$C = \frac{\Delta D}{\Delta P} \tag{2.2}$$

The upturning region in Figure 2.6 (left) corresponds to the transition between the actuation of the elastin and the collagen fibers under different pressure levels as the percentage increase in diameter to a given pressure, and is equivalent to region II in Figure 2.5.

Calculating the arterial compliance requires the measurement of the vessel diameter, the distension and the wall thickness, which can be difficult to obtain. Initially, compliance was measured using a B-mode ultrasound imaging system and an expensive vessel wall tracking system for estimation of the arterial distension [27]. Recently, J. Joseph and his team reported the proof of concept of a simpler and non-invasive *in-vivo* evaluation of arterial compliance using a single ultrasound transducer element [14]. This instrument includes a dynamic threshold algorithm to identify artery walls and uses a correlation-based tracking technique to estimate arterial distension. More information on this technique can be found in Appendix A. They performed measurements on human volunteers to assess the compliance of the carotid artery, and reported that their instrument could measure arterial distension with a precision better than 5% and with an accuracy of 1%. This technique is interesting as it allows non-invasive, *in-vivo* and fast arterial compliance measurements. It is especially used as a test to detect and predict the risk of a cardiovascular disease, as a change in compliance is often a first sign of cardiovascular diseases such as hypertension [28], atherosclerosis [29], chronic hemodialysis patients [30] and coronary heart disease [14]. Compliance is, thus, a very important property, which should be carefully analyzed for the prevention and diagnosis of cardiovascular diseases.

2.1.2.3 Viscoelasticity and fatigue

Almost all soft biological tissues exhibit a viscoelastic behavior as their constituents are viscoelastic. This means that their response is time-dependent: a different loading rate will result in a different stress-strain curve. The viscoelasticity of an artery impacts the delay of response to cyclic inflation-deflation stresses; this is known as hysteresis when changes in pressure and volume occur. This hysteresis can be seen in Figure 2.7, where the hysteresis loop for an artery and a synthetic implant is depicted. One notices also the major difference in pressure-diameter curves between a synthetic implant and an artery. The area enclosed by the hysteresis loop represents the energy loss in each cycle, which points out that an important component of the strain energy is recovered elastically each time the arterial wall is distended. This energy dissipation attenuates pressure pulses and propagates them along the arteries as waves of circumferential distention. Additionally, the viscoelastic property has been suggested to improve the fatigue life of arteries by reducing dynamic stresses and strains in the wall [4, 31].

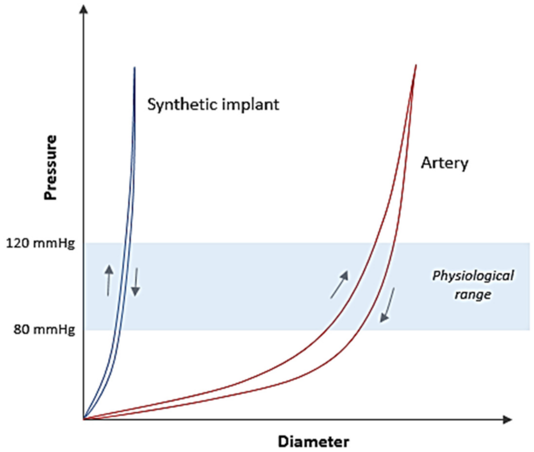

Figure 2.7: *Comparison of pressure-diameter curves between an artery (red) and a synthetic implant (blue) [4].*

2.2 Structural characterization

Understanding and visualizing the structural elements of an artery are key in the diagnostic and prevention of a cardiovascular disease, as a change in thickness or stiffness of arteries is often a sign of an underlying disease. Until recently, characterising tissue sub-structure was only done by conventional histological sectioning (2D). It has been widely used in the medical field over the years to visualize any type of tissue, organs and cells. Today, micro-computed tomography (micro-CT) is used more and more to visualize the structure of soft tissues. This technique was well known for analyzing hard tissues as it is based on differences in X-ray attenuation, but now with the use of contrast enhancing staining agents (CESAs), soft tissue can also be characterized. This technique is referred to as contrast enhanced micro-CT (CE-CT). Both techniques will be discussed more in details.

2.2.1 Histology

Histology is the study of the microanatomy of cells, tissues, and organs as seen through a microscope, and it examines the correlation between structure and function. In order to study tissues with a microscope, it is necessary to fix them, to embed them, for example in paraffin wax, and cut them into sections thin enough to be translucent. The process of fixation often consists of a chemical, formaldehyde, that crosslinks the proteins in the tissue and prevents degradation due to autolysis, and yet retain the characteristics of shape and structure. It is followed by an embedding step. The embedding process consist of a dehydration step in ethanol, followed by the replacement of ethanol by xylene. Xylene, being compatible with paraffin, enables the infiltration of the tissue with liquid paraffin. This constitutes the last step of the embedding process. Then, the tissue is cut into thin sections, typically of $5\mu m$. Finally, the tissue section can be stained, in order to accentuate specific tissue components or organelles [32]. A major advantage of histology is that the stains used can highlight specific proteins or tissue peculiarities and hence, give an idea of the protein-content present in a specific tissue, for example the protein-content of collagen. However, histological sectioning frequently induces tears, fractures, compressions and folds and, in the specific case of large arteries, often causes detachment of the adventitia layer [7]. For this reason, scientists were interested in finding an imaging technique that would not damage the tissue structure. Micro-CT is, therefore, a good candidate as it is a non-destructive imaging technique and it provides similar structural analysis to a classic histology technique.

In Figure 2.8, the difference between standard histology using light microspcopy and micro-CT is shown for the rat common carotid artery. One can see that histological sectioning technique (Figure 2.8.A) induces disrupted adventitia and holes whereas micro-CT enables visualizing structurally intact and compositionally distinct regions of an artery such as the fibrillar collagen-rich adventitia and the elastin-rich media layer at an approximate spatial resolution of 1.2 μm [7].

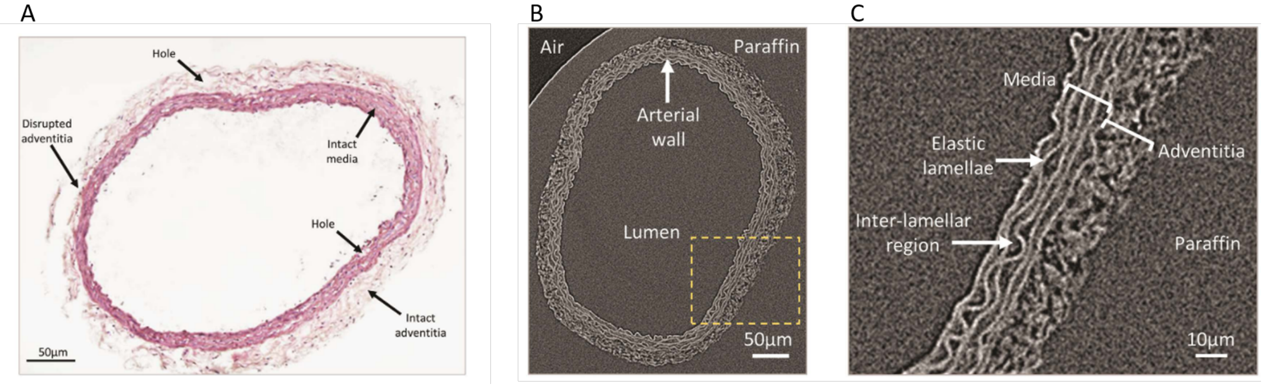

Figure 2.8: *Comparison between a histology and micro-CT technique. A: histology sectioning-induced artefacts of an artery. Light microscopy image of Hematoxylin & Eosin stained rat common carotid artery (CCA) B: Virtual slice extracted from a micro-CT dataset of an intact rat CCA (i.e. phase enhanced contrast), the yellow box indicates the magnified region in panel C. Adapted from [7].*

2.2.2 Micro-CT

Histology, as Figure 2.8 suggests, does not preserve the arterial structure and gives a 2D image of the structure only. In order to accurately characterize the structure of tissues, such as elastic arteries, it is crucial to image large regions of the vessel, while retaining the structure of the vessel intact. Moreover, in order to extract more quantitative information on the arterie wall structure, it is necessary to image the artery in three-dimensions (3D) with high resolution. Thanks to micro-CT, it is now possible to visualize the 3D morphology of biological tissues. Micro-CT is like 3D microscopy, where at very fine scale the internal structure of objects can be imaged non-destructively using X-rays. Its working principle is based on a micro-focus X-ray source that illuminates the object and a X-ray detector that collects the magnified projection images. Based on hundreds of angular views acquired while the object is rotating, the computer synthesizes a stack of virtual cross-sectional slices through the object and reconstructs the 3D volume of the object (Figure 2.9) [33].

Micro-CT is based on two principles. First, the partial absorption, meaning that X-ray photons are absorbed in the material while others are transmitted to the detector. Second, the differential absorption, meaning that different materials having different densities within the object, have different attenuation characteristics. If there were no difference in absorption levels, the sample would come out as a uniform gray level image [34].

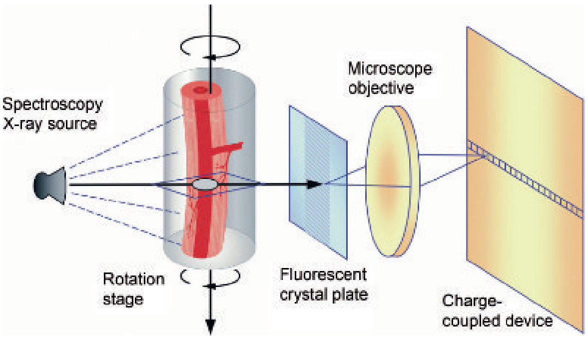

Figure 2.9: *Schematic representation of the micro-computed tomography device (micro-CT) composed of an X-ray source, a rotatable specimen stage, a scintillator, a light imaging device [usually a charge-coupled device (CCD)-based video camera], and a controlling computer [8].*

Conventionally, micro-CT is used for determining the structure of hard calcified tissues such as bone. Mineralized tissues are easy to image because they posses good attenuation properties, hence good contrast properties. The attenuation depends on the atomic number, density and thickness of the material and on the energy of the X-Ray beam. However, for soft biological tissues that posses similar density and low atomic number (low Z), their X-ray attenuation characteristics are insufficient to image their structure with high contrast. Therefore, to increase the contrast properties of soft tissues two techniques exist: phase enhanced micro-CT and contrast-enhanced micro-CT (CE-CT).

2.2.2.1 Phase enhanced micro-CT

In order to reach sufficient contrast when imaging soft tissues, phase enhanced micro-CT can be used. It consists in an imaging technique that operates with the differences in the refractive index of different materials to differentiate between structures under evaluation. It provides information concerning changes in the phase of an X-ray beam that passes through an object. It can be used to enhance edges, which allows a better visualization of soft tissues [35]. The improved contrast is attributed to both a specific tissue preparation and an improved imaging instrumentation. The tissue is prepared as for standard histology which consist of three main steps: chemical fixation, alcohol dehydration and infiltration with paraffin wax. The only difference with histology is that the sample is not cut into thin sections, neither stained to preserve the internal structure [36]. Thanks to low energy X-ray beams, a high power lens and an enhanced flat panel detector, the contrast of soft tissues can be improved.

A study of Walton and Sherratt [7] presented a sequential image processing protocol that exploits differences in X-ray opacity in order to segment the different structure of a blood vessel wall from the supporting paraffin using phase contrast enhancement micro-CT. By automatically segmenting 3D X-ray tomography volumes, they have been able to use the morphological characteristics of an artery (i.e the elastic lamellae) to segment the media from the adventitia as shown in Figure 2.10. Figures 2.8.B and 2.8.C show the image obtained of an intact rat common carotid artery (CCA) using this approach. The distinction between the three different layers that compose the aortic wall can be distinguished. However, such approaches may require complex imaging set-ups, post-processing, and long image acquisition times for laboratory instruments.

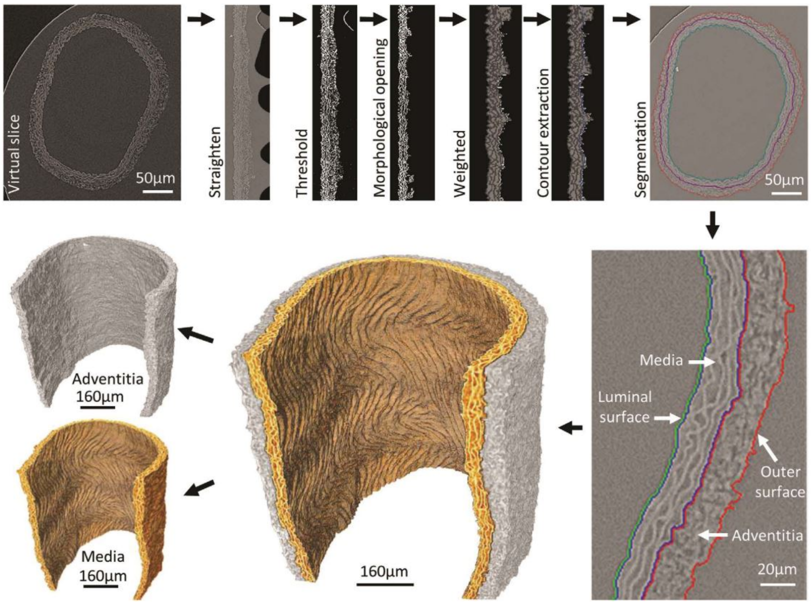

Figure 2.10: *Semi-automatic segmentation of medial and adventitial layers and elastic lamellae in large arteries. The output of the segmentation process enables the medial and adventitial layers to be virtually dissected. [7]*

2.2.2.2 CE-CT

Another way to achieve sufficient X-ray attenuation in soft tissues is the addition of chemical compounds containing high atomic number elements that bind to soft tissues. Those chemical compounds are called contrast enhancing staining agents (CESAs) and are used for CE-CT. The tissue of interest should be embedded in a CESA solution during multiple days to achieve good contrast properties. Indeed, a good contrast resides in a sufficient diffusion time to allow the CESA to diffuse in every sub-layers of the tissue. This diffusion time, also called staining time, changes for one tissue or another. It should, thus, be assessed experimentally.

Many different CESAs have been used for a large variety of soft-tissues (e.g. murine placenta [9], tendon [37], cartilage [38], bone marrow [39], blood vessels [9]). The challenge of a CE-CT technique lies in the CESA used and the staining time (i.e. the amount of time the tissue remains in the CESA solution for good diffusion). Depending on the tissue wanted to image, a CESA can be better than another and the staining time can vary. De Clercq et al., used a Zirconium substituted Keggin polyoxometalate (Zr POM) solution as CESA to visualize the vasculature structure of a murine placenta [9]. They validated Zr-POM, which allows development of the intact placenta to be visualized using CE-CT (Figure 2.11).

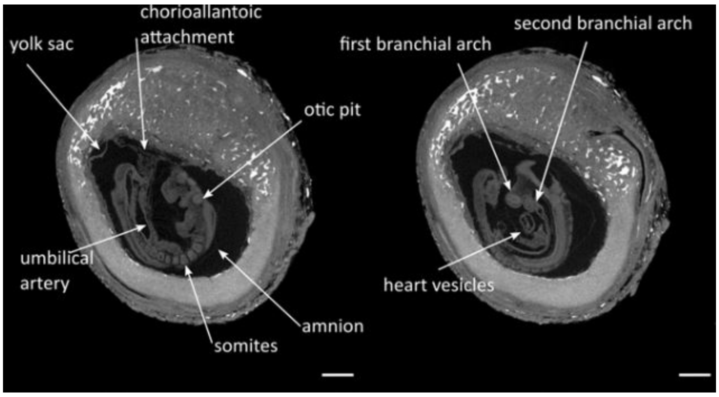

Figure 2.11: *Imaging of a murine placenta and an embryo of 9.5 days old (E9.5) with Zr-POM as CESA. CE-CT cross sections show typical features of E9.5 including chorioallantoic attachment and the presence of the umbilical artery, formation of the otic pit, the presence of the first and the second branchial arch, and the initiation of heart formation. (Scale bar: 500 μm.) Adapted from [9].*

2.2.2.3 Contrast enhanced staining agents (CESA)

S. de Bournonville and S. Vangrunderbeeck et al., recently, made a literature review on all the possible staining agents that have been used for skeletal application (cartilage, tendons and ligaments, muscle and the bone marrow) [35]. They concluded on the remaining challenges of CE-CT: a CESA should diffuse correctly in the tissue without harming or modifying the tissue structure, so that 3D CE-CT imaging technique preserves tissue structure and is non-destructive. Therefore, several CESA can be used to improve the visualization, enhance differentiation among the different layers of the arterial wall, and provide biomechanical information [40]. A good CESA must penetrate thicker tissues, differentiate between tissue components, be compatible with subsequent histology, and also be non-destructive [7].

Inorganic iodine (IKI) and iodine potassium iodide (I_2KI) are often chosen as optimal CESA for visualizing the cardiovascular system including arteries [10]. Another study showed that inorganic iodine (IKI) and phosphotungstic acid (PTA) were the gold standard CESAs for a broad range of application including vascular tissues, enabling good imaging results and simple sample preparation [41]. However, they did not study the potential destructiveness of those CESA. Indeed, IKI and PTA have, respectively, a high osmolality (i.e the number of particles of solute per kilogram of solvent [42]) and a low pH compared to biological samples and induce shrinkage of the samples which harm the samples. Shrinkage of samples is a crucial effect that needs to be avoided or minimized when using CE-CT imaging on soft tissues, as it changes the tissue morphology and integrity significantly [35]. Kerckhofs et al., reported that Hafnium-substituted Wells-Dawson POM (Hf-WD POM) could provide similar soft tissue staining as PTA, without inducing tissue shrinkage thanks to a physiological pH [37]. Hf-WD POM ($K_{16}[Hf(\alpha_2 - P_2W_{17}O_{61})_2] \bullet 19H_2O$), has a molar mass of 9472.73g/mol and for proper tissue staining a concentration of 35 mg/ml PBS was identified as sufficient.

An even more recent publication studied the staining of biological samples with 4 different POM solutions in comparison to PTA used as reference CE-CT stain. All 4 POM solutions (table 2.1) were dissolved in PBS at equal concentrations (35mg/ml PBS) and subsequently used to stain murine long bones and kidneys for CE-CT imaging: (1) Hf-WD POM, (2) Parent-WD POM, (3) Mono-WD POM and (4) Tri-WD POM. The study concluded that Mono-WD POM and Hf-WD POM showed the best diffusion and contrast-enhancement of soft tissues. Their physiological pH renders them non-destructive for soft tissues. However, Mono-WD POM is more stable in PBS than Hf-WD POM since Hf-WD POM converts and dissociates, respectively, to it. Mono-WD POM thanks to its non-destructiveness (physiological pH), chemical stability, and ease of synthesis, leading to a lower production cost in comparison with Hf-WD POM, makes it a preferred CESA for soft biological tissues [15].

Table 2.1: *Chemical structure, charge and pH of the POM species dissolved in PBS (35.0 mg/ml) [15].*

POM		Hf-WD POM	Parent-WD POM	Mono-WD POM	Tri-WD POM	PTA
Structure		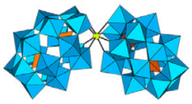	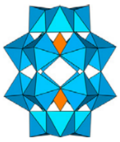	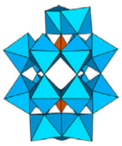		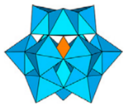
Charge	POM	−20	−6	−10	−12	−3
	Metal	+4	0	0	0	0
	Net	−16	−6	−10	−12	−3
pH		6.73	6.42	7.15	8.18	1.82

Staining time

The amount of time the tissue is incubated in the staining solution is a key factor for contrast, as both under- and over-staining have negative consequences [10]. If the tissue is prematurely removed from the solution containing the CESA, the staining will be incomplete and parts of the tissue will retain their low contrast properties when imaged. This can complicate analysis of the tissue sample; for example, automated methods of segmentation rely on each distinct layer or region having consistent intensity and can fail as a result of incomplete staining, increasing the need for manual segmentation. Conversely, if the staining time is prolonged with I_2KI, the stained tissue tends to undergo shrinkage [43]. A recent study from the university of Manchester [10] showed that an optimal staining time could be found for I_2KI for the myocardium tissue, and that a correlation exists between the staining time and the thickness of the tissue sample. They define this optimal staining time as the minimum time required to completely stain the sample while reducing the effects of shrinkage as much as possible. The thicker the sample is, the larger distance the CESA has to diffuse into the tissue, the longer the staining time will be. By plotting the intensity of each segment of a myocardium respectively with their staining time, they were able to fit these results into an equation of the form:

$$t_{stain} = A \exp(kx), \tag{2.3}$$

where t_{stain} is the required time for optimal staining of the sample, x the thickness and A & k are constant to be fitted for three different saturation levels (90%, 95% and 99%). Figure 2.12 shows their result of the fitting process in the form of a semi-logarithmic plot. Equation 2.3 is valid for myocardium samples only with I_2KI as CESA. This experiment needs to be repeated for every tissue type and for each CESA, in order to obtain a fitted relationship between the staining time and tissue type.

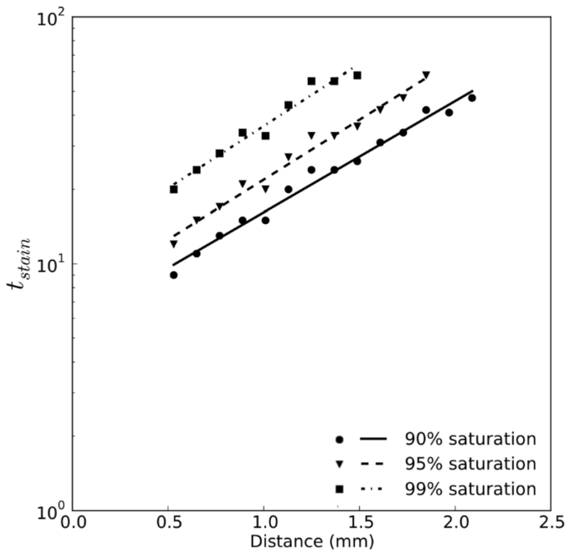

Figure 2.12: *Semi-logarithmic plot of the required staining time for different levels I_2KI saturation as a function of distance. Curves are fitted according to equation 1 and with fitted coefficients A & k [10].*

2.3 Mechanical characterization

Several mechanical tests exist to characterize biological soft tissues. Each test highlights different properties and the choice will depend on the complexity of the material. The arterial tissue is a membrane-like tissue with highly anisotropic properties. Therefore, samples can be tested as a whole or its layers can be separated to test them individually. For most mechanical tests, the deformation of the sample can be obtained by the displacement of the actuators. However, due to the possible slippage and tearing of the samples at the gripping mechanism, it is better to measure the deformation optically [11]. In the following sections, uniaxial and biaxial testing will be presented as these are the mechanical tests most frequently used on arteries. The sample shape and the mounting mechanisms will also be depicted. Then, the techniques used for strain measurement will be explained.

2.3.1 Uniaxial testing

In uniaxial tests, the load is applied in a single direction. Uniaxial tests are used to determine the failure properties of a material or to characterize isotropic materials. By themselves, these tests do not provide enough information to characterize anisotropic materials, but their simplicity is an advantage. Several uniaxial tests exist, such as strip and ring extension, indentation, pure shear, rail shear and bulge inflation [11]. The most known one is the strip extension and will be further discussed.

For strip extension tests, the sample has a rectangular or a dogbone shape of approximately 1cm by 2cm (Figure 2.13). This test is used to determine the ultimate stress or strain value where the deformation of the sample can me measured optically or estimated from the actuator displacement.

2.3.2 Biaxial testing

Uniaxial testing alone is insufficent to provide data necessary to fully characterize the mechanical behavior of anisotropic samples. Planar biaxial testing provides a convenient method of assesing

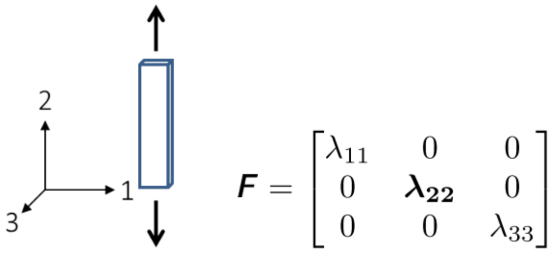

$$F = \begin{bmatrix} \lambda_{11} & 0 & 0 \\ 0 & \boldsymbol{\lambda_{22}} & 0 \\ 0 & 0 & \lambda_{33} \end{bmatrix}$$

Figure 2.13: *Conceptual sketch of the strip extension test and corresponding deformation gradient with controlled components in bold [11].*

mechanical properties of arterial vessels under loading regimes similar to those experienced *in-vivo*. In biaxial testing, two loads are applied independently on the material in two different directions. This biaxial configuration represents the best the physiological loading of biological tissues such as skin or arteries, as biological tissues are often highly anisotropic. Different biaxial tests can be obtained by varying the combination of directions in which the two loads are applied, namely, planar, extension-shear or extension-inflation as shown in Figure 2.14 [11, 44].

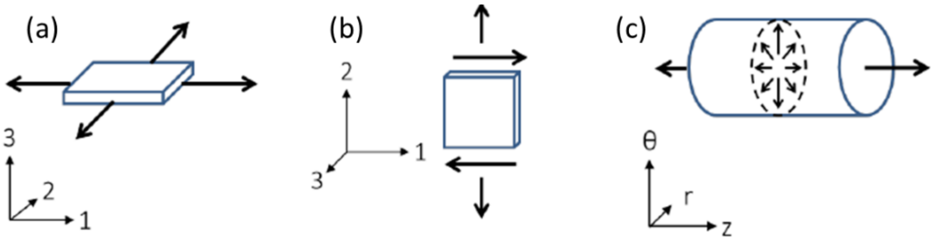

Figure 2.14: *Conceptual sketches of (a) planar biaxial, (b) extension-shear and (c) extension-inflation. Adapted from [11].*

Since this master thesis focuses on planar biaxial testing of arteries, this test is discussed in further details. As shown in Figure 2.14(a), for planar biaxial test, a thin squared sample is loaded in two perpendicular directions. This result in a plane stress state. The two loads can be varied independently resulting in different deformations.

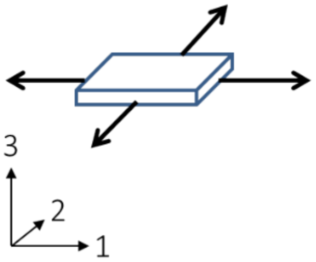

$$F = \begin{bmatrix} \boldsymbol{\lambda_{11}} & 0 & 0 \\ 0 & \boldsymbol{\lambda_{22}} & 0 \\ 0 & 0 & \lambda_{33} \end{bmatrix}$$

Figure 2.15: *Conceptual sketch of the planar biaxial test and corresponding deformation gradient with controlled components in bold [11].*

Differences in sample shape and mounting mechanism give rise to different types of planar biaxial testing (Figure 2.16). Samples can either be of squared or of cruciform shape. Often squared sample are chosen for biological tissues because of their small size and their scarcity. The sample can be clamped or attached via rakes, double sutures or pulley sutures. For arterial tissue, rakes are most often used, as they provide a uniform spacing of attachment, which restricts shear deformation of the sample. Rakes are thin needles mounted on a base. The tip of the needle is bent and pierced through the sample. Hence, loading is applied directly. Four rakes are used in a planar biaxial test, which provides a uniform spacing of the rakes and a repeatable mounting. Each rake is clamped on an actuator, which posses a loading cell. The loading cell measures the reaction force of the sample upon displacement [11].

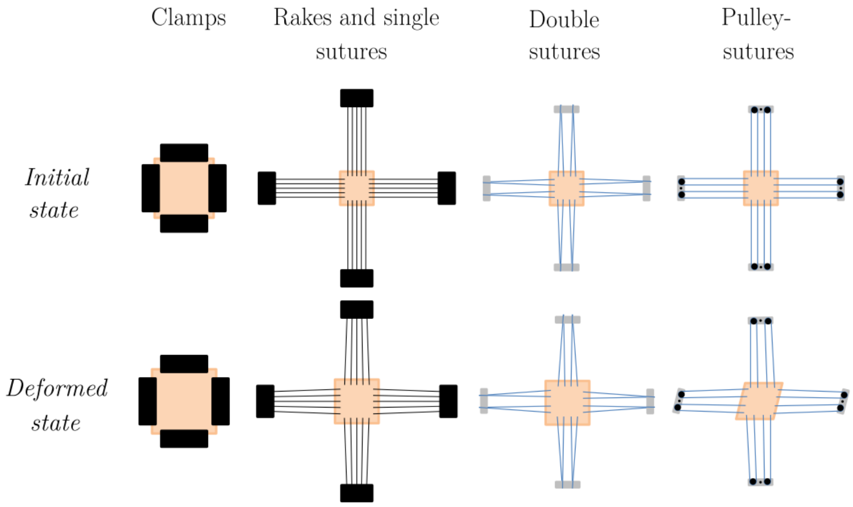

Figure 2.16: *Differences in sample shapes and mounting mechanism give rise to different types of planar biaxial testing [11].*

Strain measurement and digital image correlation

Regarding strain measurement, two major techniques exists. First, the displacement of the actuators can be used to estimate the deformation at the center of the sample. Because of slipping and tiring at the mounting site of the sample, this method is often inaccurate. Therefore, optical measurement based on markers or a speckle pattern can be used. Markers can be attached to the center of the sample; usually 4 of them are placed in square within the central 25% of the sample. A speckle pattern can be obtained using ink applied with an airbrush or using graphite powder. Digital Image Correlation (DIC) software determines the displacement of each marker or speckle from the camera images and hence, the strain field of the sample is obtained. DIC can be performed in 2D (with one camera) or 3D (with two cameras in stereoview). The size of the markers or the speckles affects the performance of the DIC system, and the speckle pattern should be as uniform as possible [11].

DIC is a surface displacement measurement technique that can capture the shape, the motion and the deformation of solid objects. The basic operation of DIC is tracking a speckle pattern in a sequence of images. The process of a DIC experiment can be divided into 3 steps:

1. Obtain a speckle pattern on the sample for tracking
2. Capture images of the sample during deformation
3. Process the acquired images with a software to obtain the strain map and displacement informations.

The processing of the acquired images is based on incremental correlation. Incremental correlation consists of comparing each image corresponding to a certain deformation state with the previously taken image state; this last one acting as a reference. DIC matches the pattern between the reference image and a deformed image or target image, and then it calculates the pattern's displacement between the reference and deformed images.

A schematic representation of the 2D-DIC principle is presented in Figure 2.17. In order to accurately calculate the displacement of point P, a subset area needs to be defined in the neighborhood around that point. Indeed, often a single pixel from the reference image cannot be reliably tracked in the target image due to the limited grayscale values. Typically, a subset of $(2M+1)\times(2M+1)$ pixels from the reference image is chosen. When the reference subset is small enough, it is assumed that each of these point $Q(x,y)$ around the subset center $P(x_0,y_0)$ in the reference subset is mapped to $Q(x',y')$ in the target subset [45]. In general, because the defined subset will not maintain its squared shape during the deformation, displacement, the subset is mapped according to the following displacement mapping functions:

$$x'_i = x_i + u + \Delta u + u_x \Delta x_i + u_y \Delta y_i \tag{2.4}$$

$$y'_i = y_i + v + \Delta v + v_x \Delta x_i + v_y \Delta y_i \tag{2.5}$$

where Δx and Δy are the distances from the subset center to point (x_i, y_i); u and v are the integer pixel displacement components; Δu and Δv are the sub-pixel displacement components of the reference subset center in x and y directions, respectively; u_x, u_y, v_x, v_y are the first-order displacement gradients of the reference subset. To evaluate the similarity between the reference and the target subset, a correlation function is defined. The correlation function used in this DIC analysis is based on the zero-normalized sum of squared difference and can be checked below [46]:

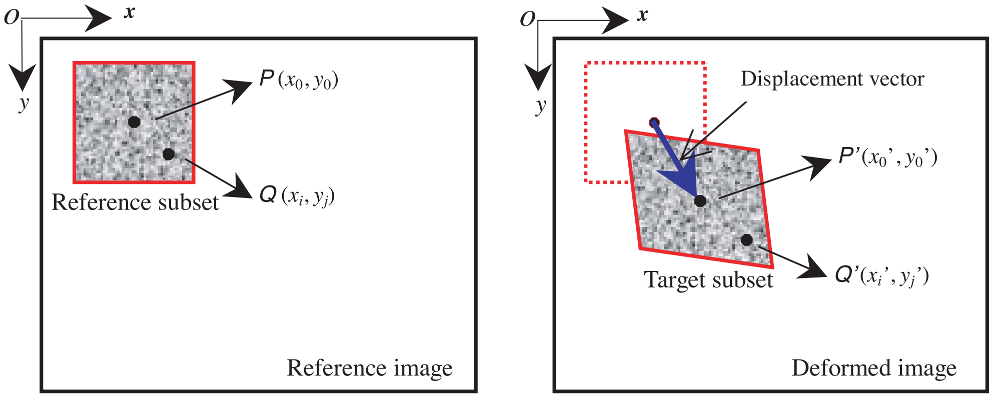

Figure 2.17: *Schematic representation of the 2D-DIC principle. The left image presents the reference state and, in the right, the deformed one. The red square indicates the subset size of point P [12].*

$$C_{ZNSSD} = \sum_{i=-M}^{M}\sum_{j=-M}^{M}\left[\frac{f(x_i,y_j)-f_m}{\Delta f} - \frac{g(x'_i,y'_j)-g_m}{\Delta g}\right]^2 \tag{2.6}$$

Where $f(x_i,y_j)$ and $g(x'_i,y'_j)$ represent the gray intensity distribution of the reference and target subsets respectively and where $f_m = \frac{1}{2M+1}\sum_{i=-M}^{M}\sum_{j=-M}^{M} f(x,y)$, $g_m = \frac{1}{2M+1}\sum_{i=-M}^{M}\sum_{j=-M}^{M} g(x',y')$ are the ensemble averages of reference and target subsets, respectively. The relationship between $f(x_i,y_j)$ and $g(x'_i,y'_j)$ is given by the linear intensity change model:

$$g(x'_i,y'_j) = a \times f(x_i,y_j) + b \tag{2.7}$$

where a is the scale factor of the intensity change, and b denotes the offset of the intensity change.

When the reference and target subsets get their maximum similarity, the minimum of the correlation function C_{ZNSSD} is reached. In other words, the gradient of C_{ZNSSD} must converge to zero. This method is called the Newton-Raphson method [12]. An equivalent method to the Newton-Raphson is the Iterative Least Square (ILS) algorithm. ILS algorithm estimates the four displacement gradients (u_x, u_y, v_x, v_y) at each point of calculation [47].

The 2D strain field estimation is made by a linear least-squares (LLS) fitting approach. LLS has a high accuracy as noise can be largely removed in the process of local fitting. Estimating the strains of a current point, can be done select a square window containing $(2m + 1) \times (2m + 1)$ discrete points (i.e., strain calculation window) around it. If the strain calculation window is small enough, the displacement distributions in it can be approximated as a linear plane:

$$u(i, j) = a_0 + a_1 x + a_2 y \tag{2.8}$$

$$v(i, j) = b_0 + b_1 x + b_2 y \tag{2.9}$$

where $i, j = -m : m$ are the local coordinates within the strain calculation window, $u(i, j)$ and $v(i, j)$ are the original displacements at location (i, j) obtained by DIC and $a_{i=0,1,2}, b_{i=0,1,2}$ are the unknown polynomial coefficients to be determined. Once they are determined, by minimizing the least-squares criteria, the three Cauchy strain components at the interrogated point can be calculated as:

$$\epsilon_x = \frac{\delta u}{\delta x} = a_1 \tag{2.10}$$

$$\epsilon_y = \frac{\delta v}{\delta y} = b_2 \tag{2.11}$$

$$\gamma_{xy} = \frac{\delta u}{\delta x} + \frac{\delta v}{\delta y} = a_2 + b_1 \tag{2.12}$$

2.4 4D CE-CT

The advantage of X-ray micro-CT over other techniques are the non-destructiveness of the samples, the minimal sample preparation required and the 3D characterization of the sample. This technique has been used for decades in the field of medicine and has recently gained popularity in material sciences thanks to improved optics and computation. The imaging resolution has now reached a level where structure at micro- and nanoscale can be studied and can be correlated to the mechanical behavior. Over the years, many ex-situ micro-CT experiments (i.e. postmorten characterization after testing) have been conducted to study the mechanical behavior of materials. However, a complete understanding of structure-property relation requires a thorough understanding of the evolution of the microstructure as function of time. This is called 4D micro-CT, where the fourth dimension is the time. Indeed, the non-destructive nature of X-ray renders it suitable for in situ experiments such that the evolution of the microstructure with the time can be quantified. Recent studies analysed the fatigue behavior of alluminium alloys and its testing in a corrosive environement [48], but also the analysis of crack opening, shear banding, fast transformation of Al-SiC composite [48], gypsum specimens [49] and TATB-PBX polymer [50]. 4D micro-CT is a very promising technique for characterizing the relationship between the mechanical behavior of different materials and their microstructure, especially in the field of soft-biological materials as in situ testing would give an insight on the microstructure of the biological sample in its physiological loaded state representing the best the *in-vivo* state. Despite a few 4D micro-CT studies on metals and polymers, its application on soft tissues has not yet been achieved due to multiple limitations and challenges.

The first limitation of soft-biological samples is the fresh state of the tissue (i.e. not fixed in formaldehyde). As soon as the tissue has been harvested, the time becomes crucial to avoid deterioration of the sample and hence a possible change in the mechanical properties of it. One way to store biological materials without further deterioration is to freeze them. However, the effect of freezing on biological tissues is not well known. Moreover, to visualize soft-biological tissues with X-rays, a CESA is needed. The samples need to be stained in a contrast enhancing solution during a certain amount of time to allow good diffusion of the stain in the sample and good contrast properties. The staining time and the temperature are crucial parameters to be optimized. Indeed, if the tissue is prematurely removed from the staining solution, parts of the tissue will retain their low contrast properties when imaged. Conversely, if the staining time is prolonged, the tissue degradation will be worse. Regarding the staining temperature, if the sample is stained at room temperature, the diffusion is enhanced and the time needed for obtaining good contrast is reduced. However, the deterioration of the sample is faster. Contrarily, if the sample is stained at 4°C the deterioration is limited, but the time needed to obtain good diffusion of the CESA is lengthened, and a longer staining time could also harm the tissue. Stewart et al., used a preservation solution of protease inhibitors, antibiotics, and antimycotics in addition to their CESA, to avoid the deterioration of their tissue sample during the experiment. It allowed to stain the tissue during a longer time and enabled good diffusion in an ex-vivo human lip cartilage, and good contrast properties [51]. Furthermore, the concentration, the acidity and the osmolarity of the CESA also need to be optimized to avoid any change in the microstructure and hence a change in the mechanical properties of the investigated sample. A 4D contrast-enhancement CT technique to characterize soft-biological tissue is possible if the staining and the preparation of the tissue does not affect significantly the mechanical properties of it.

3

Problem statement, aim and objectives

A full characterization of soft tissues should include the structural analysis, while the tissue sample is mechanically loaded. Indeed, soft-biological tissues such as arteries, are constantly subjected to a physiological load in their *in-vivo* state. Analyzing the evolution of the micro-structure as function of time and characterizing the relationship between the micro-structure and the mechanical behavior would be a huge breakthrough. 4D CE-CT can be used for this purpose. For this a CESA is needed to improve the contrast of the tissue. Its effect on the mechanical properties of soft tissues and the staining time required to obtain good contrast properties are, yet, not known. A trade-of needs to be find between the time required to fully stain the tissue and the temperature at which the samples are stained. In this master thesis, the focus will be on two CESAs, the Hf-WD POM and the Mono-WD POM. Their physiological pH, good diffusion and excellent contrast properties make them ideal CESAs for soft tissues. The staining temperature will be fixed at room temperature and the staining time, only, will vary.

The aim of this master thesis is two-fold. First, to characterize the micro-structure of arterial tissue using 3D CE-CT imaging and Hf-WD POM as CESA. Secondly, to assess the effect of Hf-WD POM and Mono-WD POM on the mechanical properties of arterial tissues. To do so, planar biaxial testing will be used. By comparing the results obtained for a control group and stained groups, the effect of Hf-WD POM and Mono-WD POM on the mechanical behavior of soft-tissue will be assessed. Moreover, as the staining time is decisive for the degradation of the tissue, a preservation solution, which purpose is to slow down the degradation of the tissue, will be used in combination with a CESA. Its effect will be assessed. Those constitute crucial information for the realization of 4D CE-CT.

The general aim of this work can be translated into the following objectives:

1. Micro-structural characterization (3D CE-CT)
    - Defining an image analysis protocol for Hf-WD POM based CE-CT images of arterial tissues.
    - Characterizing the general parameters of arteries such as the inner and outer diameter of the aorta and of the media layer, the mean lumen surface and the cross-sectional thickness.
    - Analyzing the elastin lamellae present in the media layer because this layer defines the mechanical behavior of an artery, and furthermore, characterizing the structure separation, meaning the distance in between the elastin lamellae, the structure thickness and the number of elastin lamellae present.
2. Effect of Hf-WD POM on the mechanical properties of arterial tissues

- Analyzing the mechanical properties of control tissue samples (i.e. not stained) using planar biaxial tests.
- Analyzing the mechanical properties of stained samples using planar biaxial tests.
- Analyzing the mechanical properties of stained samples with the addition of a preservation solution using planar biaxial tests.
- Comparing the Cauchy stress obtained for the control samples with the stained samples.
- Assessing the effect of the preservation solution on the samples and compare it with the control samples.

4

Microstructural characterization

To better understand the microstructure of blood vessels, it is essential to visualize them using contrast-enhanced micro-CT (CE-CT). Once scanned, an image analysis protocol can be defined for Hf-WD POM based CE-CT images of arterial tissues. Thanks to this protocol, the structural parameters of the blood vessel can be calculated. This allows to quantitatively characterize its micro-structure: the mean lumen surface, the inner and outer diameter of the aorta and of the media layer, the crossectional thickness and the structure separation distribution of the elastin lamellae. In this master thesis, the focus will be on characterizing the micro-structure of a rat thoracic aorta stained with Hf-WD POM.

4.1 Materials and methods

4.1.1 Sample preparation

The sample is a thoracic aorta, coming from a laboratory rat. Once harvested, the sample was fixed in a 4% paraformaldehyde solution (Sigma Aldrich, USA) during 24 hours at 4°C. Then, the sample was immersed in a contrast enhancing staining agent (CESA) at 4°C for 48 hours. The CESA used is an in-house prepared 3.5% Hf-WD POM solution (35mg/ml PBS). The sample was placed on a shaker plate to improve the diffusion of the CESA in the aortic tissue. After staining, the sample was scanned with CE-CT.

4.1.2 CE-CT - image acquisition

Before scanning, the sample was slightly dried in a tissue to remove the excess of wet and then, wrapped in parafilm to avoid the sample from drying. It was placed on a sample holder and inserted in a Phoenix Nanotom M (GE Measurement and Control Solutions, Germany) to scan the sample. Due to the relatively high X-ray attenuation of POM stained samples, a diamond coated tungsten target was applied. For the rat thoracic aorta, a voltage of 60 kV, a current of 70 μA was selected. The exposure time was 500 ms, and 2400 images were acquired over 360° using the long scan mode (frame averaging = 3; image skip = 1). A 1.1 μm isotropic voxel size was selected. After the scan, the CE-CT images were reconstructed using the Phoenix Datos|x CT (GE Measurement and Control Solutions) software with a beam hardening correction of 7 and a Gaussian filter with radius of 3 voxels.

4.1.3 CE-CT - image processing and analysis

The dataset obtained after reconstruction, is composed of 2395 crossectional images of the rat thoracic aorta. To process and analyze this dataset, three softwares were used: DataViewer, CTAn and CTVox (Bruker Micro-CT, Kontich, Belgium). The software Dataviewer provided a 3D visual inspection, as well as qualitative inspection of the rat thoracic aorta. This program displays reconstructed results as slice- by-slice orthogonal projections. With CTAn, a morphometric analysis on the aorta and on the elastin fibers has been performed. 3D rendering of the datasets has been obtained thanks to CTvox software. Those softwares are often used for characterizing bone morphology. The objective of this analysis was, therefore, to define a protocol in order to extract general parameters on the morphology of first, a rat aorta, but which could then serve to characterize many other arteries or blood vessels.

An artery is composed of three distinct layers: the adventitia, the media and the intima. It is, therefore, interesting to measure the inner and outer diameter of the artery and also of the media layer, which is the thickest one. The crossectional thickness of the aorta and media layer, and the mean luminal surface (i.e. inner surface) are also interesting parameters to obtain for a full characterization of the arterial microstructure. Table 4.1 summarizes the morphometric parameters calculated for the rat thoracic aorta, and their descriptions. Moreover, the elastin fibres or lamellae found in the media layer of an artery play a very important role in its mechanical behavior. By using a right threshold, it was possible to segment only the elastin lamellae from the rest of the aorta structure, in order to perform an analysis on the elastin fibers only. Table 4.2 describes the morphometric parameters calculated on the elastin lamellae in the media layer.

Table 4.1: *Morphometric parameters selected for the analysis on the aorta via the software CTAn, and their description [16]. Due to artefacts in the adventitia, two parameters could only be assessed for the media layer.*

Morphological analysis on the aorta

Parameters	**Description**
Inner diameter [μm]	The mean equivalent circle diameter of all discreet 2D objects in a single crossectional image slice.
Outer diameter of the media [μm]	The mean equivalent circle diameter of all discreet 2D objects in a single crossectional image slice.
Mean luminal surface [μm^{-1}]	The ratio of the available surface over the entire lumen volume.
Mean thickness of the media [μm]	The mean thickness calculated for every slice.

Table 4.2: *Morphometric parameters selected for the analysis on the elastin lamellae via the software CTAn, and their description [16].*

Morphological analysis on the elastin lamellae

Parameters	**Description**
Structure thickness [μm]	Average elastin fibers thickness measured as the mean diameter of consecutive spheres that fill the structure.
Structure separation [μm]	The thickness of the spaces between elastin fibers.
Volume Fraction [%]	The volume of elastin fibers over the total volume of the media layer.

4.1.3.1 Image analysis protocol

Before performing the morphological analysis, the raw dataset was prepared; the first and last hundred of crossectional images were removed from the dataset due to too large artefacts (i.e. cone beam arterfacts) and underexposure as shown in Figure 4.1, then specific regions or volume of interest were defined within the software.

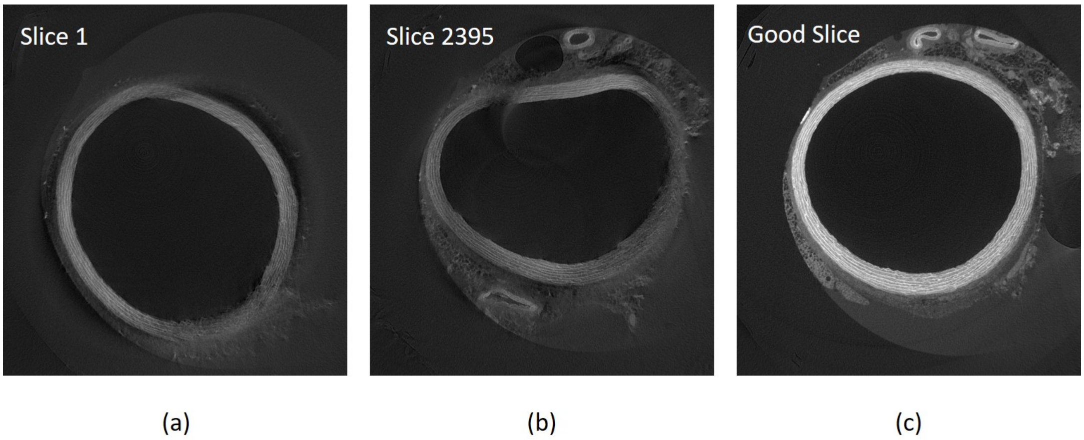

Figure 4.1: *Images a and b correspond to the first and last slice of the dataset. Due to a bad exposition and artefacts present, the hundred first & last slices of the dataset should be removed before performing the analysis. Image c represent a good slice where the exposure is uniform, which allows a good morphometric analysis.*

Indeed, depending on the parameter selected, the Region of Interest (ROI) on which the software computes, will change. Therefore, three ROIs were defined as shown in Figure 4.2:

(a) Inner ROI: the yellow circle and its inside to calculate the inner diameter and lumen surface.

(b) Outer ROI: the red circle and its inside to calculate the outer diameter of the media layer.

(c) Donut ROI: to calculate the thickness of the media layer and within this ROI, the elastin lamallae were segmented in order to calculate all the parameters mentionned in Table 4.2.

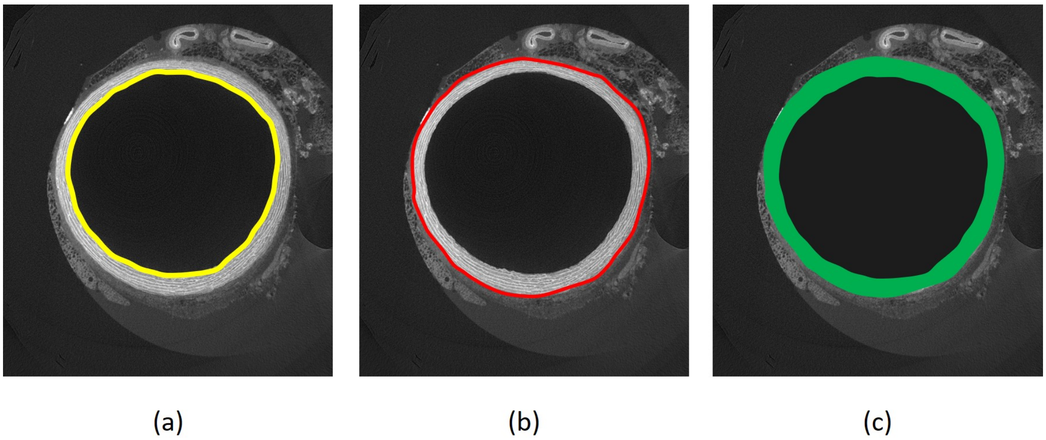

Figure 4.2: *The three regions of interest drawn to perform a morphological analysis on it: (a) the inner ROI, (b) the outer ROI, (c) the donut ROI.*

The outer and donut ROI are only drawn arround the media layer, because the adventitia was too disrupted to precisely draw it within the ROI. Therefore, the outer diameter and the thickness of the aorta will only be measured visually using CTAn and not through the morphological analysis performed by this software.

Once the ROIs have been drawn within the software CTAn, the following image analysis protocol was used for the three ROIs:

1. Image filtering (Gaussian filter) applied onto non-binarised (i.e. non-thresholded) images in order to obtain a smoother image, with less noise.
2. Selection of a threshold to segment the initial image in only two grey values: white and black. The white part fill the region of interest drawn and will be taken into account for the morphomological analysis. The black part represents the outside of the ROI, which will not be taken into account when calculating the morphometric parameters.
3. Morphological operation:
    (a) Closing to connect objects that are in close proximity but initially distinct on the image.
    (b) Shrink-wrap to stretch the ROI over holes, because holes in the arterial structure can be present on certain slices.
    (c) Despeckling to remove black speckles, it fill the space occupied by the region of interest of the aorta.
4. 2D and 3D analysis to obtain the morphometric parameters selected.

For the morphological analysis on elastin lamellae, it was necessary to choose a threshold that only highlighted the elastin fibers (Figure 4.3). Therefore, a threshold of 172 was applied. However, due to inhomogeneities present in the contrast properties of the slices, only a quarter of the aorta was selected and taken into account for the analysis. By inhomogeneity, it is meant that the elastin lamellae do not appear with the same white intensity everywhere in the aorta, which makes the lamellae indistinguishable from one another in certain regions of the aorta. To avoid errors, a new square ROI was selected on the previous donut ROI to only calculate the morphometric parameters, where elastin fibers can be distinguished from one another.

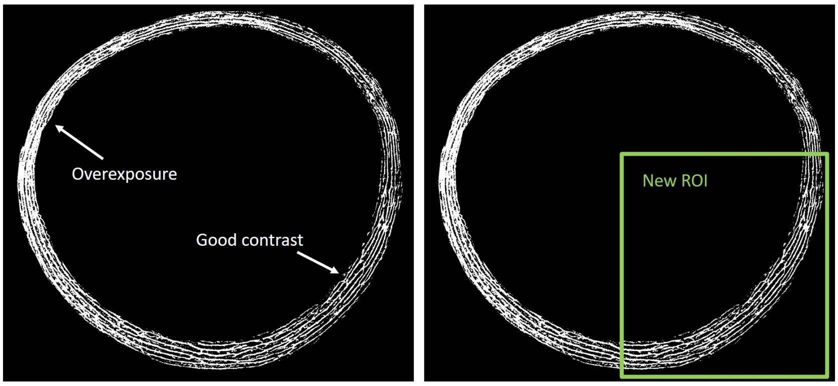

Figure 4.3: *A threshold of 172 is applied to segment the elastin lamellae from the rest of the aorta. However, due to oberesposure in certain regions of the aorta, elastin lamellae can't be distinguished. Therefore, a new square ROI is defined for the morphological analysis.*

4.2 Results and Discussion

4.2.1 Visual inspection

An artery is composed of three distinct layers: the intima, the media and the adventitia. These three layers can be observed in Figure 4.4. Figure 4.4a shows a 3D view of the rat thoracic aorta stained with Hf-WD POM, while the Figure 4.4b presents the three orthogonal views of such tissue.

The main structural components of an aorta are the elastin and the collagen. In the specific case of a rat thoracic aorta, the elastin to collagen ratio is estimated to 2.5 according to Keith et al, [52].

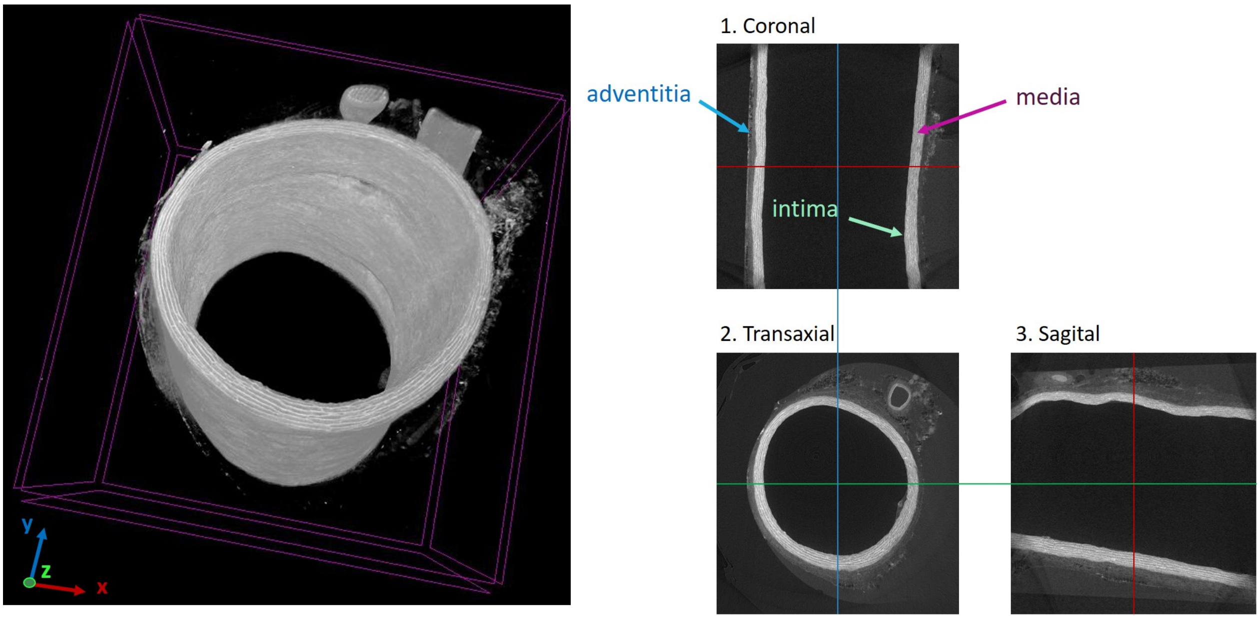

(a) *3D view of the rat thoracic aorta* ***(b)*** *Orthogonal views of the rat thoracic aorta*

Figure 4.4: *(a) 3D view of the rat thoracic aorta and (b) three orthogonal views of the thoracic aorta cross- section indicating the different layers, from inside to outside intima, media and adventitia.*

The intima, the innermost and thinnest layer, is barely observable on the CE-CT slice. This layer consists of simple squamous epithelium and a thin basement membrane, which provides a smooth surface for the blood circulation. This layer is so thin (only some tens of microns thick), that it cannot be distinguish from the media layer as it approaches the spatial image resolution of the CE-CT images. Even with standard histology, it is difficult to observe this layer. Figure 4.5 shows a histology slice of another thoracic rat aorta stained with hematoxylin and eosin. On this figure, the intima can neither be distinguished from the media. However, the media layer is well observable with its elastin lamellae and the adventitia is clearly observable, even though it is highly damaged and disrupted.

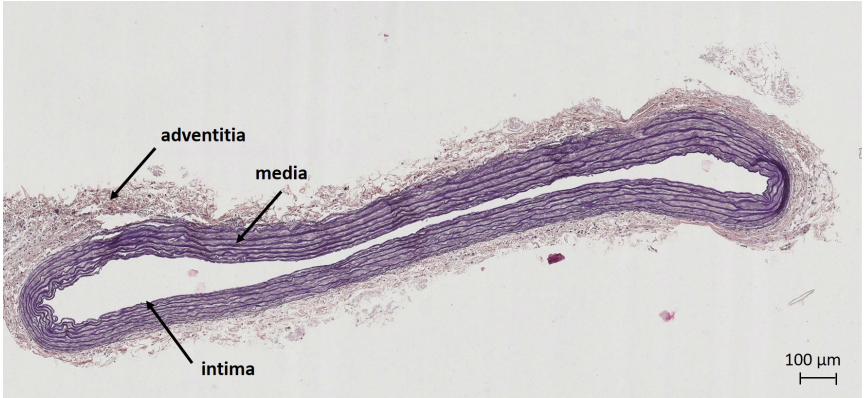

Figure 4.5: *Histology slice of a rat thoracic aorta stained with hematoxylin and eosin (HE).*

The media layer, the thickest layer and the one playing the most important role in the mechanical behavior of the artery, is visible in light grey (Figure 4.4). It is composed of circumferentially and coherently aligned elastin fibers, smooth muscle cells and collagen fibers. It provides the contraction force to impulse the bloodstream through the body. The elastin fibers appear white on the CE-CT slice. Thanks to the good contrast properties of elastin fibers under Hf-WD POM stain, morphological analysis on the elastin lamallea could be performed. The adventitia, the outermost layer, is clearly distinguishable in Figure 4.6. At certain regions, it seems damaged and disrupted, potentially because of the starting degradation of the tissue. It is mainly composed of dense collagen fibers and a basal membrane. However, the collagen fibers cannot be distinguished from the basal membrane, probably due to too similar densities and attenuation properties, hence it possesses the same grey level. Moreover, a secondary artery is distinguished, and will further connect to the thoracic aorta as it can be seen in Figure 4.4a.

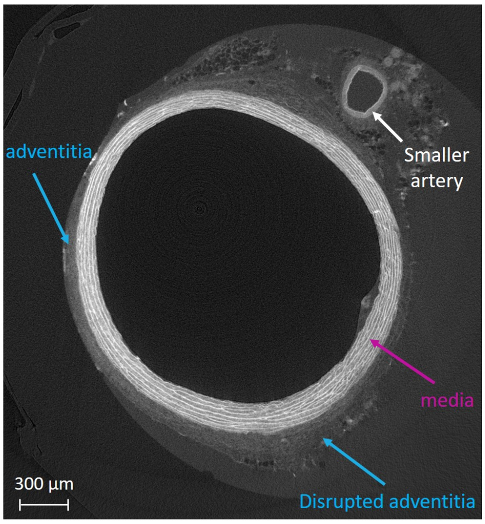

Figure 4.6: *Transaxial slice of the rat thoracic aorta stained with Hf-WD POM. The media and the adventitia are observed. A secondary artery is visible, it will further connect to the thoracic aorta.*

It is possible to asses visually the inner and outer "diameter" of the aorta and of the media layer. As the aorta is not a perfect circle, it is, actually, the distance between two opposite points that is measured, as shown in Figure 4.7. For the inner diameter calculation, the distance is the same for the aorta and the media layer as the intima layer is only a couple tens of microns thick. However, for the outer diameter, one takes into account the adventitia for the outer diameter of the aorta which is not the case when measuring the outer diameter of the media layer. This measurement was repeated for every hundred slices where the mean values are 1 620 μm for the inner diameter, 1 880 μm for the outer diameter of the media and 1 978 μm for the outer diameter of the aorta. The upper and lower limit values for the inner and outer diameter both for the media layer and the aorta are given in the Table 4.3.

Figure 4.8 shows the variation of the inner and outer diameter values along the thoracic aorta when moving away from the heart. One can see that there is a decreasing trend when moving away from the heart. Indeed, the inner and outer diameter decrease as we move along the slices of the dataset. The outer diameter plot measured for the media layer is almost a parallel to the inner diameter plot, both decreases together with the same intensity. However, the plot of the outer diameter of the aorta is a bit more rough and does not follow the two other curves as nicely. This is probably due to the lack of precision when measuring the outer diameter of the aorta as the adventitia is highly dirsrupted at the bottom right, hence knowing exactly where the adventitia stops is very difficult. However, the general decreasing tendency is in agreement with the study of Erbel et al [53] and of Moini et al [54]. Erbel studied the aortic dimensions in human subjects of the ascending and descending aorta and concluded that the size of the aorta decreases with distance from the aortic valve in a tapering fashion.

Table 4.3: *Upper and lower limit of the rat thoracic aorta. The upper limit corresponds to the closest slice from the heart and the lower limit to the furthest slice from the heart.*

Boundaries	Inner diameter [μm]	Outer diameter (media) [μm]	Outer diameter (aorta) [μm]
Upper limit	1 722	1 986	2 092
Lower limit	1 534	1 799	1 908

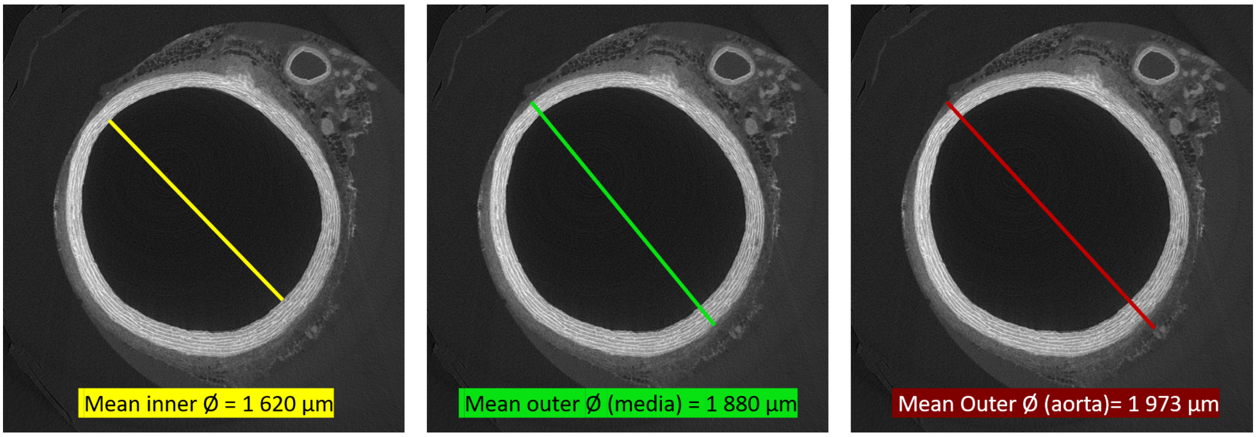

Figure 4.7: *Visual inspection gives the distance that separates two opposite points, which can be interpreted as the inner diameter and outer diameter of the media layer and the aorta: 1 620 μm, 1 880 μm and 1 973 μm respectively.*

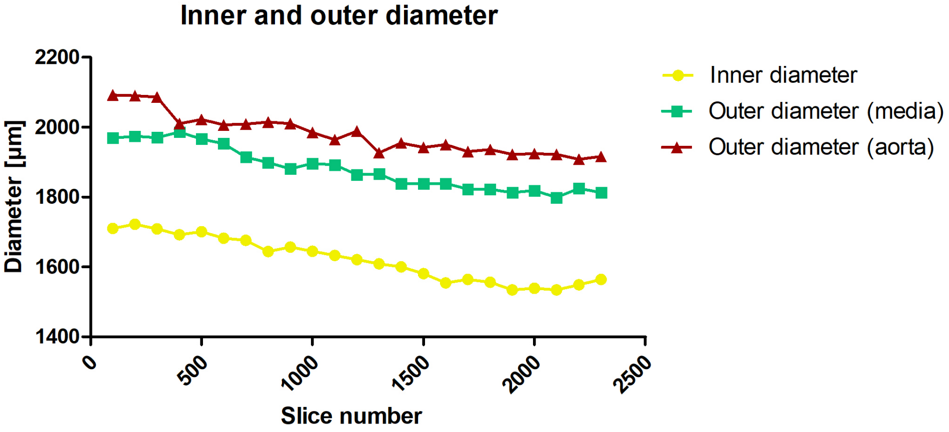

Figure 4.8: *The inner diameter and outer diameter of the media and aorta decrease when moving away from the heart. Slice 1 is the slice the most proximal to the heart and slice 2395 is the slice the most distal to the heart. The simple linear regression equations for the inner and outer media diameter were $y = -0.092 \times x + 1731$ and $y = -0.088 \times x + 1986$, respectively.*

Knowing the mean diameters, we can calculate the thickness of the media layer and of the aorta by subtracting the inner diameter to the outer diameter, respectively, and dividing by two. The media layer possesses, then, a mean thickness of 130 μm and the mean thickness of the aorta is equal to 176.5 μm. This means that the thickness of the adventitia is around 45-50 μm.

Based on the binarized images that segment the elastin from the rest of the media layer, it is possible to count the number of fibers it contains. By looking at a zoom, 6 to 8 fibers can be counted in the transverse direction (Figure 4.9). This measurement was repeated for every hundred slices, at 3 different location as shown on Figure 4.9. The mean number of fiber lamellae is equal to $6.80 \approx 7$. This is in agreement with the histology section (Figure 4.5) of another rat thoracic aorta, where approximately 6-7 fibers can be counted. A study of Clark et al, measured with standard histology the mean number of lamellae in the mouse aorta and obtained a value from 5.67 ± 0.1 to 4.17±0.1, with a noticable decrease when moving away from the heart [55]. Göktürk et al, analyzed aortic elastic lamellae in mice with histology and obtain a mean value of 6 lamellae for the media layer [56]. A value of 6.8 elastin fibers for the rat aorta seems, thus, plausible. Figure 4.10 shows the amount of fibers counted for every hundred slices. However, no noticable decrease of the number of fibers is seen as we move away from the heart.

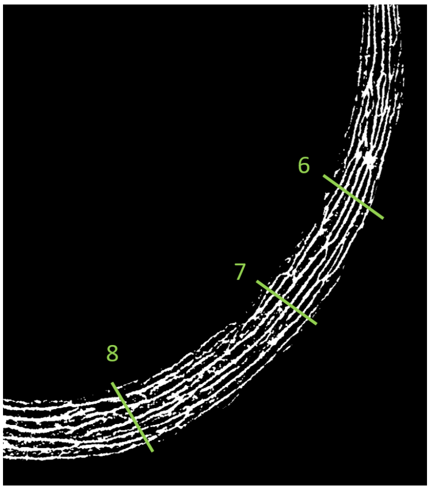

Figure 4.9: *The number of elastin lamellae running through the media layer can be counted. There is approximately 6 to 8 fibers in the media layer of this rat thoracic aorta stained with Hf-WD POM.*

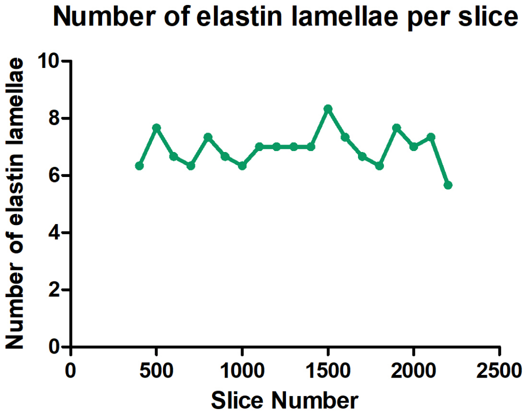

Figure 4.10: *The number of elastin lamellae were counted at three different location for every hundred slices. A mean value of 6.8 elastin lamellae has been obtained.*

4.2.2 2D & 3D Morphological analysis

4.2.2.1 Aorta

Table 4.4 shows the result for the 2D morphological analysis performed via the software CTAn on the aorta. However, certain parameters were only calculated for the media layer such as the outer diameter and the crossectional thickness. Indeed, the adventitia was too disrupted to be taken into account in the ROI drawn.

Table 4.4: *Morphometric parameters and their values calculated by CTAn on the rat thoracic aorta stained with Hf-WD POM.*

Parameters	Value
Inner diameter	1 502 μm
Outer diameter of the media	1 697 μm
Luminal surface	3.8 $\times 10^{-3}$ μm^{-1}
Thickness of the media	98 μm

Inner and outer diameter of the media

Values of 1 502 μm and 1 697 μm have been obtained using CTAn for the inner and outer diameter of the media, respectively. By comparing this result with the one obtained by visual inspection, the mean inner and outer distances are equal to 1 620 μm and 1 880μm. This gives a difference of 118 μm and 183 μm, respectively, for the inner and outer diameter. This difference can reside in the method that CTAn applies to calculate the diameter. It calculates the mean equivalent circle of the aorta for all slices and take the diameter of this mean equivalent circle, whereas with visual inspection, a distance is measured, which is closer to the major axis of an ellipse, rather than the diameter of a circle. Moreover, the software calculates for all slices the equivalent circle diameter and takes the mean afterwards, whereas with the visual inspection one analyzed the diameter for only a couple of slices.

It is possible to compare these results with the literature. Often, only the mean outer aortic diameter was given and no comparison were made between the inner and outer diameter, neither between the outer aortic and outer medial diameter. Therefore, only the mean outer diameter of the media layer will be compared with the literature, by omitting the thickness of the adventitia, which was not taken into account in the CTAn computation. A study of Trachet et al, measured and compared the outer murine abdominal aorta dimensions *in-vivo*, both with ultrasound and micro-CT. They concluded that both micro-CT and ultrasound are reliable methods to assess murine outer aortic diameters [57]. Their measured values are in the same range than the one obtained in this study. Eventhough, they measured the abdominal aorta (AA) diameter, which is the segment of the aorta below the thoracic segment and not the thoracic aorta (TA) as done in this study, it is possible to compare their proximal value for the AA diameter with the one for the TA. Their values lies between 1 000 - 1 300 μm for the outer diameter. As they measured the AA diameter, it is logic to find values lower than for the TA because it is known that the diameter of an aorta decreases when moving away from the heart. Moreover, they measured the diameter in murine animals and not in rats, which could also explain the lower values. Those values are also in agreement with another study, that compared three ultrasound-based methods to assess the aortic diameter of murine animals [58]. Furthermore, a study of Wheeler et al, measured, with histology, the murine thoracic aorta diameter and its variation with aging [59]. However, their diameter values are half the one measured in this study with CE-CT, and they reported an increase in the diameter of a 100 to 150 μm, as the animal ages from 6 to 21 months. Unfortunately, the age of the rat used in this study is not known, which could potentially partially explained this difference. Another reason could be that histology can damage the aorta, and its circular shape might flatten as seen in Figure 4.5, which renders it more difficult to asses the diameter.

We can conclude that CE-CT is an accurate method to measure the aortic diameter, as also proven by Trachet [57]. Moreover, it allows to assess both the inner and the outer diameter of the media layer, which until now only the mean outer diameter has been mentioned in the literature.

Thickness of the media layer

The thickness of the media layer was calculated based on the donut ROI and gave a thickness of 98 μm. Moreover, by subtracting the inner diameter to the outer diameter calculated previously by CTAn, and then, by dividing by two a value of 97.5 μm (Eq 4.1) is obtained. It shows that both calculation performed are convergent. Furthermore, if one does the same calculation but with the mean diameter visually assessed, one obtains 130 μm (Eq 4.2). It is slightly higher, but this difference can be understood by the difference of method of calculation as mentioned earlier and also, by the imprecision of the visual measurement.

$$\text{CTAn:} \qquad \frac{\varnothing_{Outer} - \varnothing_{Inner}}{2} = \frac{1697 - 1502}{2} = 97.5\mu m \tag{4.1}$$

$$\text{Visually:} \qquad \frac{\varnothing_{Outer} - \varnothing_{Inner}}{2} = \frac{1880 - 1620}{2} = 130\mu m \tag{4.2}$$

Two different studies conducted on murine animals converge towards the same values of 80-100 μm for the aortic wall thickness. One uses histology [59], the other one uses phase contrast microscopy [60] to determine the aortic wall thickness. One can conclude that the image protocol analysis for the thickness of the media layer is correct as it gives a value of 98 μm, which is similar with the values found in the literature.

Luminal surface

The luminal surface is calculated as the ratio of the surface over the entire lumen volume and not as an absolute value. The reason for this is that, with an absolute value, one cannot compare this specific surface value with other vessels or other aorta from different species, because if the volume of the vessel increases, so does the surface. A ratio allows to take this into account and enables comparison. This ratio is equal to 3.8 $\times 10^{-3}$ μm^{-1} in the case of the rat thoracic aorta.

Measuring the luminal surface with CE-CT can be interesting for stent application. Indeed, to obtain good stent apposition, the stent, once inflated via a balloon, should achieve the size of the ideal diameter of the reference vessel. This requires to know the patient's vessel size. So far, intravascular ultrasound (IVUS) and optical coherence tomography (OCT) have been used for determining this value, however due to cost and time consideration, these techniques are rarely used as a routine manner [61]. Moreover, the minimal luminal diameter is a key indicator for stenosis, and restenosis if a stent has already been applied [62]. Assessing this minimal luminal diameter, allows to determine the percentage of stenosis and the potential need of reintervention in case of restenosis. Furthermore, when applying a stent, often, overexpansion to a larger oversized diameter is required to ensure full stent apposition [63]. For this latter, different stent and dilatation balloon size exists. Therefore, knowing the luminal surface of the patient may help to choose the correct stent and inflation required to achieve good stent apposition and avoid restenosis. This could lead to a more patient-specific approach.

To conclude, CE-CT allows to measure the luminal surface, which is expressed in this study as the ratio of the available surface over the entire lumen volume. This enables comparison with other species or other vessels. Moreover, assessing the luminal surface could be very interesting for stent application to reduce restenosis and the need of reintervention.

4.2.2.2 Elastin lamellae

Characterizing the elastin lamellae could be very interesting for modeling applications. Indeed, so far the most used material model for arterial tissues is the Gasser-Odgen-Holzhapfel (GOH) model. It takes into account two fiber families, namely collagen I and collagen II [64]. However, it does not account for elastin lamellae present in the media layer. By quantitatively assessing the number of elastin lamellae present in the media layer, their thickness, their volume fraction and their structure separation, it could help generate a new material model that accounts both for collagen fibers and elastin lamellae. Table 4.5 shows the result for the 3D morphological analysis performed via the software CTAn on the elastin lamellae.

Table 4.5: *Morphometric parameters and their values calculated by CTAn on the elastin lamellae segmented from the rest of the media layer.*

Parameters	**Value**
Structure thickness	6.41 μm
Structure separation	13.27 μm
Volume Fraction	27.8 %

Structure thickness

The mean thickness of an elastin fiber is equal to 6.41 μm in this study. The elastin fiber thickness distribution on the whole dataset can also be plotted (Figure 4.11). In the literature, multiple studies measured the elastin fiber thickness via standard histology [63], multiphoton laser scanning microscopy [55], multiphoton excitation fluorescence microscopy and computational image processing [65]. All of them were converging towards a value of 2.7 - 3 μm, half the value calculated by CTAn. All measured the lamellae thickness of murine animals and one made the comparison between mice and rats aorta, and no significant difference in the lamellae thickness was observed [65]. None of those studies used a CESA to obtain the lamellae thickness. Could Hf-WD POM be the reason of a swelling of the fibers that could explain such a difference ? Another reason could be that with histology and multiphoton laser microscopy only a couple slices are analysed, and by looking at the structure thickness distribution, 8% of the volume corresponds to a thickness of 2.5 - 3 μm. Moreover, with histology one uses ethanol for a dehydration step, this dehydration step often induces shrinkage of the tissue, which can explain the lower values obtained in the literature. Furthermore, in this study, one has used a threshold to segment the elastin lamellae. This threshold was manually assessed and could also contribute to the higher structure thickness obtained in this study. All these reasons can potentially and partially explain the difference seen between this study and the literature.

Structure separation

The structure separation, meaning the distance between elastin fibers is equal to 13.27 μm. The structure separation distribution can also be plotted (Figure 4.12). Unfortunately, no studies assessing this parameter were found, so no comparison with the literature could be done. However, multiple studies report the number of elastin fibers in the media layer of murine animals to be equal to 6 [55, 56], their thickness to be equal to 2.7-3 μm [65, 63] and the media thickness to lie between 80 - 100 μm [59, 60]. Based on those number, on average the structure separation can be

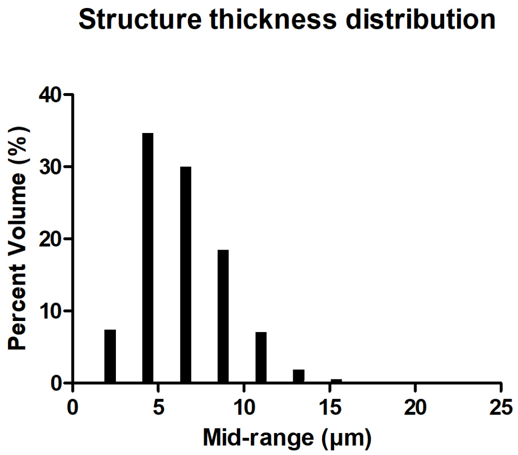

Figure 4.11: *Structure thickness distribution of elastin lamellae in the media layer of rat thoracic aorta stained with Hf-WD POM. The mean value is equal to 6.41 µm.*

calculated as:

$$\frac{\text{Media Thickness} - \text{Number of fibers} \times \text{Thickness of fibers}}{\text{Number of fibers}} \approx \frac{90\mu m - 6 \times 3\mu m}{6} = 12\mu m \qquad (4.3)$$

12 μm is not too far away from the value calculated by CTAn. 13,27 μm seems a plausible value for the structure separation.

An advantage of CE-CT is that it can calculate a distribution over the length of the aorta instead of giving only absolute values at one location as done in other studies. Figure 4.12 gives the distribution of structure separation between elastin lamellae. It ranges from 2 μm to 25 μm with a maximum in percent volume around 15 μm.

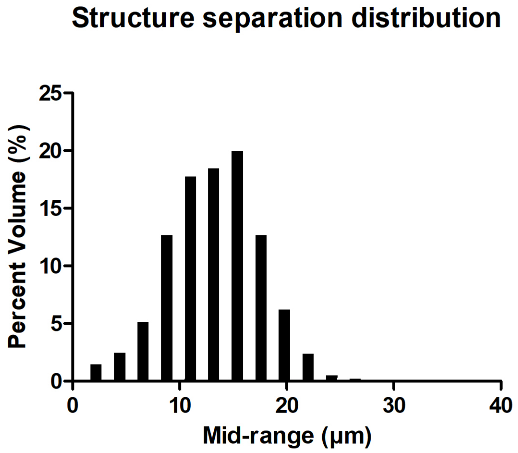

Figure 4.12: *Structure separation distribution of elastin lamellae in the media layer of rat thoracic aorta stained with Hf-WD POM. The mean value is equal to 13.27 µm.*

Volume fraction

The volume fraction represent the volume of elastin lamellae over the total volume of the media layer. The elastin lamellae are segmented from the media, so that the rest of the media is seen as a void and only the white elastin lamellae are taken into account in the computation. This gives an idea of the elastin content in the media layer. The volume fraction of elastin lamellae in the media layer is equal to 27.8 % in the case of a rat thoracic aorta. One can compare this value with the literature. A study of Saatchi et al, used immunofluorescent array tomography to characterize the volume fraction of elastin. They obtained a value of 25% to 30% for the volume fraction of elastin present in murine aortas [66]. Another study using histology obtained values ranging from 35% to 40% for murine thoracic aortas [59]. One can conlude that 27.8% for the volume fraction of elastin of a rat thoracic aorta is plausible.

4.3 Conclusion

An image analysis protocol has been determined for a rat thoracic aorta stained in Hf-WD POM, which is capable of fully characterizing the microstructure of an aorta. Indeed, the inner and outer diameter of the aorta, its thickness and luminal surface were determined and the values match the values found in the literature. Moreover, thanks to the good staining properties of elastin lamellae with Hf-WD POM, it has been possible to characterize the elastin content, the structure thickness and the structure separation, parameters rarely assessed by CE-CT in the literature, but for which, matching values have also been found in the literature with other visualization techniques. Characterizing the elastin lamellae could be used for computer models of arteries, as until now only collagen fibers are taken into account in arterial models, such as the GOH model. Although, only one sample of a rat thoracic aorta has been analysed, the potential of structural characterization with CE-CT has been showed. Indeed, the luminal surface and the inner diameter of an aorta are important parameters for stent applications and thanks to the non-destructiveness of CE-CT, it could make it an ideal visualization technique for more patient-specific therapeutic approaches.

5

Influence of staining

In order to assess the effect of Hf-WD POM and Mono-WD POM on the mechanical behavior of arteries, different sample groups have been tested and compared. Sample acquisition was randomized to ensure that any differences between and within the groups were not systematic at the onset of the experiment. Planar biaxial tests have been used to characterize their mechanical properties. Thanks to strain mapping and DIC analysis, it was possible to identify the reaction force and the Cauchy stress, and to compare these properties between the different sample groups.

5.1 Materials and methods

5.1.1 Sample preparation

Axial strips were extracted from the upper part of a porcine descending aorta as shown in Figures 5.1 & 5.2. Tissues have been obtained from the slaughterhouse. Immediately after harvest, samples were transferred to the lab for preparation. The samples for biaxial testing were 10 mm by 10 mm. The right upper corner of every sample was cut in order to remember the orientation (i.e circumferential and axial direction) of the sample (Figure 5.1). As soon as the samples have been harvested, they were put in physiological solution (phosphate buffered saline or PBS) and were stored at -80°C to prevent the degradation. Before testing them mechanically, they were thawed overnight at 4°C. The sample preparation protocol was as followed:

(i) **Tissue harvesting:** Porcine thoracic descending aorta is harvested at the slaughterhouse and immediately stored in PBS at room temperature until their arrival at the lab.

(ii) **Sample preparation:** The aorta is cut according to the randomization principle in 10 samples of 10x10 mm using a scalpel on a mat for soft tissue. The top right corner is cut for orientation tracking. All connective tissue should be carefully removed without damaging the adventitia and intima layer (i.e. the two outer layers). Drying of the samples should be avoided by always pouring physiologic solution on the samples.

(iii) **Tracking of sample:** Each individual sample will obtain a FIBEr ID (i.e a bar code with a unique series of 10 digits) for sample tracking.

(iv) **Storage:** Individual samples are stored in PBS in eppendorf tubes at $-80°C$ to avoid degradation.

(v) **Thawing:** Prior to performing a mechanical test, samples need to be thawed over-night at 4°C.

(vi) **Staining:** Depending on which group the sample belongs to, an extra step of staining in a CESA solution or a preservation solution or in PBS is required before testing. All sample groups, except the control group, are stained in their respective solution at room temperature and on a shaker plate for better diffusion of the solution, during the amount of time foreseen.

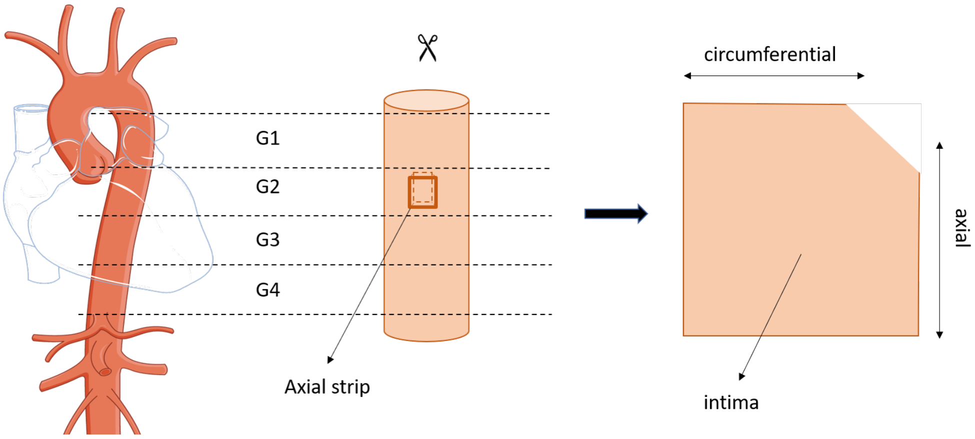

Figure 5.1: *Dissection of the porcine descending thoracic aorta into four subsection (G_1, G_2, G_3 and G_4) for a randomization process, and sample orientation.*

In total, six porcine thoracic descending aortas have been harvested. Per aorta, 10 biaxial samples have been collected. In order to assess the influence of Hf-WD POM and Mono-WD POM on the mechanical properties of porcine aorta tissues, 8 different conditions have been tested. Per condition, 6 to 8 biaxial samples have been prepared. Depending on the condition, samples have been immersed in four different solutions. The protocol to prepare those solutions can be found in the appendix C. Two solutions were the two different CESAs with a staining time of 72h, and of 120h also for Mono-WD POM. The third solution was PBS for sham samples, where they have been aged in this solution for 72h and 120h. The fourth is a preservation solution to assess its effect on delaying the degradation of the sample (staining time of 120h).

1. **Control group:** unstained samples. They were tested immediately after thawing.
2. **Sham 72h group:** after thawing, samples were immersed in PBS during 72h.
3. **Sham 120h group:** after thawing, samples were immersed in PBS during 120h.
4. **Stained 72h Hf-WD POM group:** after thawing, samples were stained in a solution of 3.5% Hf-WD POM during 72h.
5. **Stained 72h Mono-WD POM group:** after thawing, samples were stained in a solution of 3.5% Mono-WD POM during 72h.
6. **Stained 120h Mono-WD POM group:** after thawing, samples were stained in a solution of 3.5% Mono-WD POM during 120h.
7. **Preserved 120h group:** after thawing, samples were immersed in a preservation solution containing 5 mM ethylenediaminetetraacetic acid (EDTA), 5 mM benzamidine HCl and 5× antibiotic−antimycotic [51], during 120h.
8. **Preserved & stained 120h group:** after thawing, samples are immersed in a mixed solution of 3.5% Mono-WD POM and the preservation solution [51] during 120h.

The circumferential and axial Cauchy stress of those 8 groups have been computed and compared using a multiple t-test for statistical analysis. This will be further detailed in section 5.1.8.

5.1.2 Sample randomization

As mentioned in section 2.1.1, mechanical properties of an aorta can slightly change upon the location on the descending branch. Therefore, it is important to randomize sample extraction along the descending aortic branch, so that samples from one group are not systematically taken from the same location neither from the same animal. This ensures that any differences between and within the groups are not systematic at the onset of the experiment. For this matter, once a porcine thoracic descending aorta was harvested, it was divided into 4 sections, namely G_1, G_2, G_3 and G_4. This allowed to allocate 10 different samples per aorta, on the 4 different regions as shown in Figure 5.2. This cutting protocol was repeated for the 6 aortas (i.e. 60 samples), so that each group was constituted of 6-8 samples coming from the 6 different animals and from the 4 different G regions.

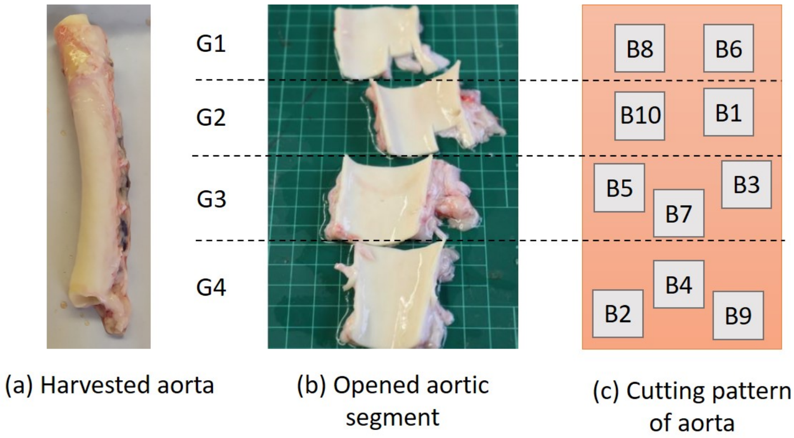

(a) Harvested aorta (b) Opened aortic segment (c) Cutting pattern of aorta

Figure 5.2: *A randomization process is achieved by separating the aortic segment into four G regions and by allocating the 10 biaxial samples on every harvested porcine aorta so that, each group is constituted of 6-8 samples coming from the 6 different animals and from the 4 different G regions.*

5.1.3 Thickness measurement

The sample thickness was measured via a micro-laser scanner. The Gocator 2300 (LMI technologies) has been used for this project and allowed to measure the local thickness of the sample using a laser displacement sensor without applying any force to the sample. This is an advantage in comparison to a caliper measurement, where the force applied on the sample is unknown and can differ between different samples. The sensor delivers robust 3D inspection across a wide range of high-speed, high-volume applications. It has a maximum resolution in the z axis of $1.8 \mu m$, and in the x axis of $14 \mu m$. The field of view ranges between $18 - 26\ mm$ [67]. The sample is placed on a smooth ground plate, and the laser renders a grayscale surface image (Figure 5.4), and a comma-separated values file. These output files are processed by implementing a Matlab code. In a first step, the data is visualized in a scatter plot as seen in Figure 5.3, to determine whether and where the sample is curled due to residual stresses, which could lead to wrong measurements. In a second step, the grayscale image is used to select a region of interest (ROI) where the sample lays flat on the ground plate. Based on this ROI, the thickness of the sample can be calculated by subtracting the known plate height.

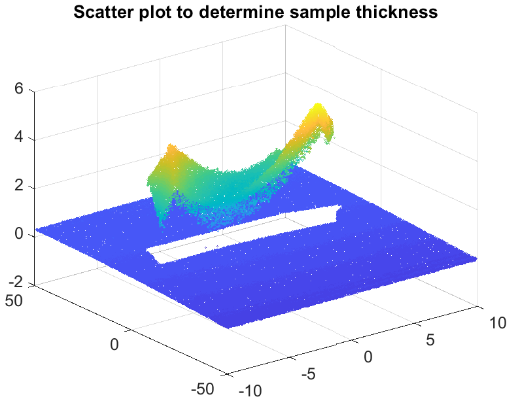

Figure 5.3: *Scatter plot showing a sample curvature due to residual stresses*

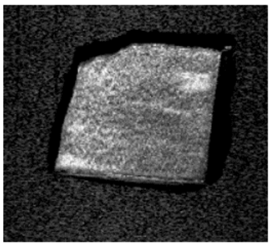

Figure 5.4: *Grayscale image of aortic sample.*

5.1.4 Planar biaxial testing

5.1.4.1 Device

All the samples were tested with a Messphysik-Zwick/Roell planar biaxial testing machine specialized for the mechanical testing of soft tissues, as shown in Figure 5.5. With this testing machine, both uniaxial and biaxial tests can be performed.

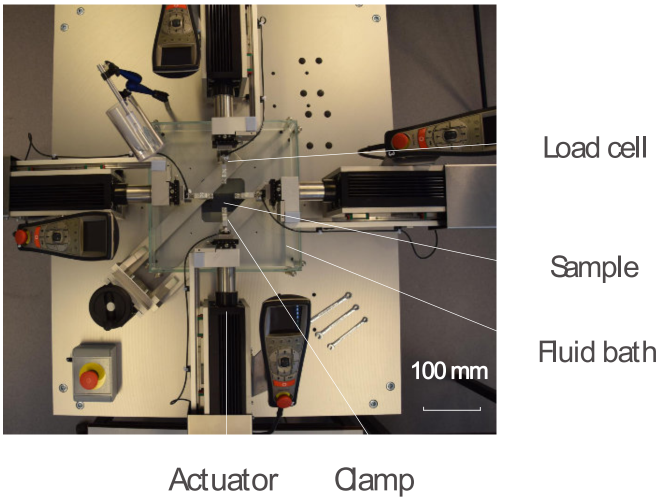

Figure 5.5: *Messphysik-Zwick/Roell testing machine. Planar biaxial test utilizes 4 actuators to impose force or displacement on the sample in two directions. The fluid bath is filled with physiological solution to prevent the drying of the sample and possess a heating system to heat the physiological solution to* 37°C. *Adapted from [13].*

For planar biaxial tests, the Messphysik-Zwick/Roell tester imposes force or displacement along two perpendicular directions, using four independent actuators and load cells. The mounting system used was rakes to ensure a uniform loading of the sample. Each rake is composed of 5 high-quality stainless-steel needles of 0.3 mm of diameter, 3 mm of depth and 1.25 mm spacing between each needle, as shown in Figure 5.6. Rakes provide a uniform spacing, which restricts shear deformation of the sample.

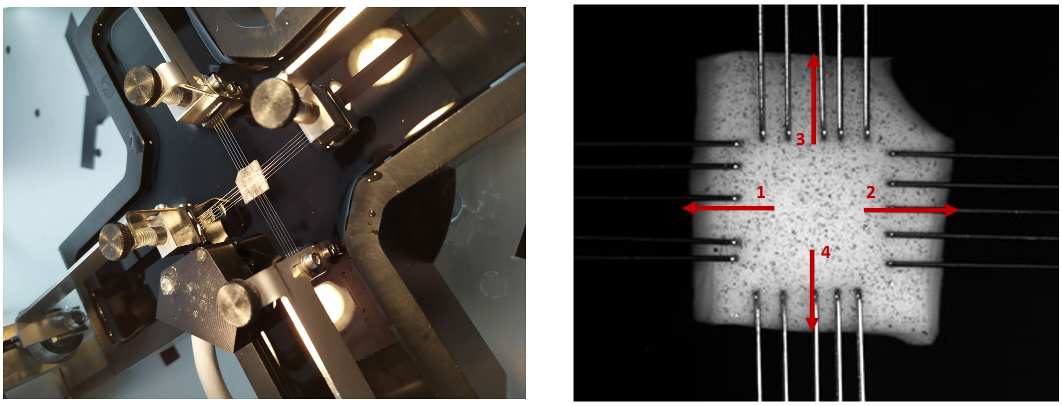

(a) *Sample mounted* ***(b)*** *Zoom on the rakes*

Figure 5.6: *Planar biaxial testing set-up. Four rakes of 5 needles allow a biaxial loading of the sample. (a) The sample is immersed in physiological solution at* 37°C *to avoid drying of the sample. (b) Numbers 1,2,3 and 4 are the notation for the different loading cells. 1 and 2 will be considered x axis, the equivalent circumferential direction in the vessel, and 3 and 4 y axis, the axial direction.*

The testing machine possesses four high-resolution linear drives, which can be displacement- or force-controlled completely independently from one another. For the current study, displacement-control was performed. Force measurement is achieved via the load cells. The load measuring range of the load cells lies between 0.8 and 200 N with a relative accuracy of load signal of 0.5% of nominal load. However, below 0.8 N the accuracy of the load signal decreases to 1-2% [68].

5.1.4.2 Software

The testXpert II operates the Messphysik-Zwick/Roell tester both under planar biaxial and uniaxial tensile tests. The software allows the user to implement the experimental protocol and to select among displacement or force-control, preload, preload speed, initial position of the rakes or sampling rates. Also, the load level, the relative load ratio between the two perpendicular load directions and the testing speed are controlled through the program. The software generates, after each experiment, the reaction forces of the load cells and the displacement of the rakes from the reference.

5.1.5 Experimental protocol

All the samples tested in this study were subjected to a displacement-controlled experimental protocol. As a result, they were stretched in the x (circumferential) direction and the y (axial) direction according to the following steps:

1. **Mounting:** Samples were mounted using rakes. The orientation of the sample was kept such that the circumferential and axial direction were aligned with the test axes x and y, respectively.

2. **Liquid bath and testing temperature:** All samples were immersed in a PBS solution during testing and the temperature of the solution was set at 37°C to better replicate the *in-vivo* conditions. Indeed, the testing temperature affects the mechanical behavior of soft tissues: aortic tissues tend to become slightly more compliant as the temperature increases [69].

3. **Preload:** A small preload was applied to avoid sagging of the samples. Indeed, once the sample is extracted from their *in-vivo* cylindrical configuration and is cut, internal stress is

released. Preloading allows to analyze the true properties of arteries by applying a small initial load to reach the initial *in-vivo* stretched configuration.

4. **Preconditioning:** When performing mechanical tests, an important phenomena can occur and needs to be taken into account, namely stress softening. This is a phenomenon observed in an *in-vitro* test, where the response changes after the first couple of cycles of the same loading. This effect is due to the viscoelastic properties of arteries. After several loading cycles, the response becomes repeatable and this repeatable behavior is assumed to be the *in-vivo* behavior. Due to the softening effect, the load is thus applied during multiple cycles until the behavior is repeatable. This is referred to preconditioning.

5. **Loading magnitude:** Because the loads that an artery can withstand are not always predictable, loads are applied with an increasing magnitude at a set testing speed. This ensures that enough data is collected per sample tested. Five loading steps were applied on each sample with an increasing magnitude, from 5% to 25% of deformation with a 5% step size. The loading magnitude 5% corresponds to strain of 5%.

6. **Loading ratios:** Different loading ratios can be applied, meaning the ratio between the loading applied on the x-axis and on the y-axis in planar biaxial test (e.g. 1-1, 0.5-1, 1-0.5). However, in this study only the 1-1 loading ratio has been applied.

Those 6 steps were repeated five times in order to reach a maximum load of 25% at the end of the loading step 5. The output contains the four forces measured at the gripping mechanism, the position of the gripping mechanism and the pictures for the strain measurement (see section 5.1.6). Table 5.1 summarize the experimental protocol and gives the experimental conditions.

Table 5.1: *Experimental protocol for biaxial planar test using the testXpert II software.*

Biaxial Planar Test Protocol

Loading step	Preload [N]	Preload speed [mm/s]	Load [%]	Ratio	Preconditioning: Number of cycles	Testing Speed [mm/s]
LS1	0.05	0.1	5	1-1	5	5
LS2	0.05	0.1	10	1-1	5	5
LS3	0.05	0.1	15	1-1	5	5
LS4	0.05	0.1	20	1-1	5	5
LS5	0.05	0.1	25	1-1	5	5

5.1.6 Strain mapping and digital image correlation

To perform digital image correlation, a camera was used (Manta G-917 B, Allied Vision Technologies GmbH, Stadtroda, Germany). It is an industrially used monochrome charged-coupled device (CCD) camera type that incorporates the high-quality Type 1 (15.972 mm diagonal) Sony ICX814 CCD sensor with EXview HAD II technology. At full resolution, this camera runs 10.1 frames per second. With a smaller region of interest, higher frame rates are possible. To conduct 2D-DIC analysis, one camera was placed above the mounted sample, perpendicular to it. The distance between the camera lens and the sample was approximately 30 cm. This led to a field of view (FOV) of 26.4mm by 21.14mm.

The Vic-Snap 8 software enables the camera configuration. The user interface shows a view of live images of the mounted sample. Once the test is started in the testXpert software, the camera starts capturing images with a speed of around 20 images/s. The focus of the cameras is manually defined. Also, the aperture of the cameras and the light incidence must be selected so the image does not present overexposure spots. In this experiment, two additional LED lamps were used to adjust the luminosity and lighten correctly the sample.

Strain mapping calculation was based on digital image correlation (DIC). The basis operation of DIC is tracking a speckle pattern in a sequence of images as explained in section 2.3.2. The speckle pattern corresponding to a ROI is divided into subsets by the DIC analysis software. A subset is a portion of the speckle pattern that is selected for tracking. It is an important parameter for the DIC analysis, and for the current analysis a subset size of 41 pixels have been chosen. To obtain a speckle pattern on the luminal side of the artery, graphite powder was, first, deposited on a sheet of paper. By shaking the paper, a uniform coverage of the graphite powder was obtained. Then, the intima layer of the sample was deposited on this sheet of paper covered with graphite powder (Figure 5.7). It is important to uniformly distribute the graphite on the sample to obtain an accurate strain analysis after image processing.

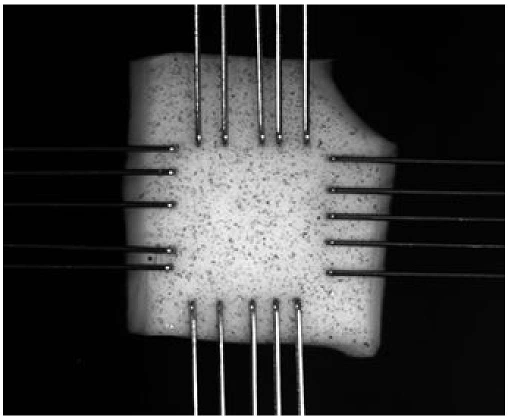

Figure 5.7: *Porcine aortic sample mounted in the biaxial tester with graphite speckles applied.*

For this project, the software used to calculate the strain map was VIC-2D. It is a turnkey solution that utilizes optimized correlation algorithms to provide full-field two-dimensional displacement and strain data for mechanical testing on planar specimens. The VIC-2D system can measure in-plane displacements and strains over 2000% with measurement resolution as low as 10 micro-strain possible [70]. Their correlation algorithm is not applied for every pixel of the image. In practice, the next pixel for which the strain will be defined is located at a certain distance from the previous pixel. This distance is defined by the step size. For the current analysis, the default value (7 pixels) was used, as suggested by the VIC-2D software. Figure 5.8 shows the output after strain map calculation where the calculation area, also called ROI, is specified for the strain calculation. The selected ROI is a square, that lies in between the rakes. It corresponds to only the central 25% of the area in between the rakes to avoid edge effects of the rakes [44].

The DIC output, i.e. strain map, is transformed to a deformation gradient **F**, using the selected ROI. **F** represents the relation between the deformed and undeformed sample and shows the deformation in the three direction (Equation 5.1).

$$\mathbf{F} = \begin{bmatrix} \lambda_{11} & \lambda_{12} & 0 \\ \lambda_{21} & \lambda_{22} & 0 \\ 0 & 0 & \lambda_{33} \end{bmatrix} \tag{5.1}$$

λ_{ii} represents the stretch in the circumferential direction (11) and in the axial direction (22). λ_{12} and λ_{21} are the shear components. Assuming incompressibility of aortic samples $det(\mathbf{F}) = 1$, λ_{33} can be written as $\frac{1}{\sqrt{\lambda_{11} \cdot \lambda_{22} - \lambda_{12} \cdot \lambda_{21}}}$, where λ_{11} and λ_{22} will be used for the stress calculation.

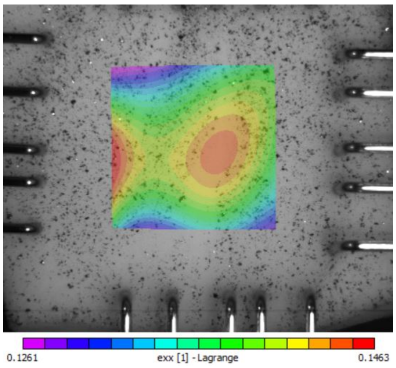

Figure 5.8: *Strain computation of a porcine aorta sample via the software VIC-2D.*

5.1.7 Stress calculation

The stress calculation was performed using a Matlab code created and kindly provided by Dr. ir. Heleen Fehervary and ir. Klaas Vander Linden (Soft Tissue Biomechanics group, Biomechanics Section, Dept. of Mechanical Engineering, KU Leuven). The code calculates the experimental Cauchy stress and first Piola-Kirchhoff stress, and then plots the results for the loading cycle selected. It also allows to compare the experimental results with the ones obtained using the Gasser-Ogden-Holzhapfel (GOH) material model and optimises the data for such model. This material model is frequently used to model arterial tissues and computes a strain energy function that accounts for collagen fibers dispersion. The strain energy function is expressed through 5 parameters: C_{10} [MPa], k_1 [MPa], k_2 [-], κ [-], α [rad]. C_{10} and k_1 are stress-like parameters indicating the stiffness of the ground matrix and the collagen fibers. k_2 is a dimensionless parameter representing the non-linear hyperelastic behaviour at high strains. κ is the dispersion of the collagen fibers and α is the angle between the mean fiber direction of one fiber family and the circumferential direction [71, 72]. More on the GOH model can be find in the Appendix B. In this master thesis, the focus will be on the experimental stresses obtained for each group of samples tested and the comparison between those eight groups will be discussed.

The Cauchy stress $\boldsymbol{\sigma}$ or true stress is the stress in the current configuration, while the first Piola-Kirchhoff stress $\boldsymbol{P}$ or engineering stress is the stress in the reference configuration. The Cauchy stress is more relevant, but it is easier to measure the underformed area in experiments and thus the first Piola-Kirchhoff stress is calculated as the reaction force RF_{ij} measured by the load cell (deformed configuration) per reference area:

$$P_{ij}(t) = \frac{RF_{ij}(t)}{A_{0,j}} \tag{5.2}$$

where RF_{ij} is the force in the i-th direction acting on area with normal in the j-th direction and $A_{0,j}$ is the undeformed area with normal in the j-th direction [11]. As planar biaxial tests are performed, no radial component is determined, assuming $RF_{33}(t) = 0$. Therefore, the first Piola-Kirchhoff stress becomes:

$$\mathbf{P}(t) = \begin{bmatrix} \frac{RF_{11}}{A_{0,1}}(t) & 0 & 0 \\ 0 & \frac{RF_{22}}{A_{0,2}}(t) & 0 \\ 0 & 0 & 0 \end{bmatrix} \tag{5.3}$$

$A_{0,1}$ and $A_{0,2}$ are the result of multiplying the sample thickness with the sample length between the rakes at the starting point of the test. The Cauchy stress is related to the first Piola-Kirchhoff stress and can be calculated as:

$$\boldsymbol{\sigma} = J^{-1}\mathbf{P}\mathbf{F}^T \tag{5.4}$$

where J the jacobian is calculated as the determinant of the deformation gradient ($J = det(\mathbf{F})$) matrix and $\mathbf{F}$ is the deformation gradient. A preload correction is applied to compensate for the sample mounting onto the rakes, which results in non-zero forces before the start of the test at a stretch 1. Therefore, a linear extrapolation is applied on the stress-stretch curve to make sure that the stretch is not 1 for the initial non-zero stress. Note that different methodologies to compensate for the preload effect exists, and are currently being investigated by the supervising research group.

5.1.8 Statistical Analysis

For statistical comparison of the axial and circumferential Cauchy stress between the different conditions, multiple t-tests have been used with the correction for multiple comparisons using the Holm-Sidak method. Indeed, comparing the results of the 72h and 120h stained and sham groups, respectively, allows to identify the differences in the mechanical properties due to the staining. In addition, comparing the properties of the control group and of the two sham groups enables to identify the changes in properties that are due to sample aging and sample degradation. A potential difference between the two CESAs used can also be assessed. Moreover, the effect of the preservation solution can be analysed by comparing the preserved 120h group with the sham 120h group, and also the preserved & stained 120h group with the stained 120h Mono-WD POM group. The value of significance or p-value selected as a reference for the analysis was 0.05. The statistical software used to perform the analysis was GraphPad (Prism 8.1.1, California, United States). For all graphs, the notations in Table 5.2 are used to indicate the level of significance.

Table 5.2: *Notation to indicate the level of significance.*

Significance	P value
ns	$P \geq 0.05$
$*$	$P \leq 0.05$
$**$	$P \leq 0.01$
$***$	$P \leq 0.001$

5.2 Results and Discussion

5.2.1 Maximum applied load

The experimental protocol was defined such that multiple loads starting at 5% to 25%, corresponding to equivalent strain, have been applied on the sample. However, for all stained samples, demounting was seen when approaching the loading step 20%, hence the 20% strain. More specifically, the rakes detached from the sample, hence the experiment has been stopped before the end of the experimental protocol. Therefore, only the circumferential σ_{11} and axial σ_{22} Cauchy stresses, up to the 15% strain, have been calculated, and will be compared for the different conditions tested. This correspond to the loading step of 15% and of stretch 5. Figure 5.9a and 5.9b show the outcome of the experiment for a control sample and a stained sample, respectively. The control sample was stopped at the end of the experimental protocol (25% load), whereas the stained sample demounted at the load 20%, which prevented the continuation of the experiment. The blue frame represents the stretch 5 at load 15%, which has been analysed for all samples, because it ensures that at this stretch the arterial behavior is repeatable, hence it characterizes the *in-vivo* behavior.

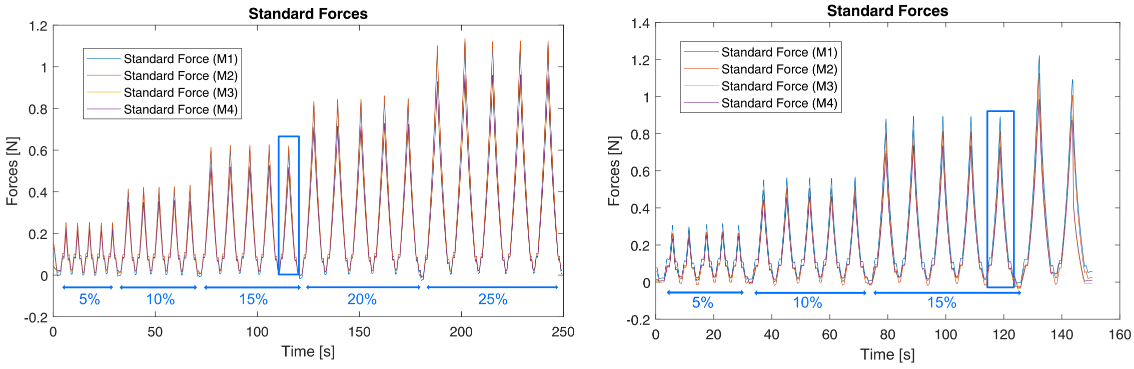

(a) Control sample

(b) Stained sample

Figure 5.9: *The outcome of the planar biaxial Messphysik-Zwick/Roell tester give the forces sensed by the 4 load cells (M1, M2, M3 and M4) in function of time. (a) For the control sample, no demounting was observed, hence the test stopped at the end of the experimental protocol. (b) For a stained sample, it demounted at the cycle 2 of the load 20%, hence the experiment has been aborted there.*

5.2.2 Thickness of the samples

The thickness of the samples was measured via a micro-laser just before the testing, thus, after the immersion of the samples in their respective solution. Therefore, it can be interesting to compare the thickness of the samples to assess whether certain solutions (i.e. preservation solution, CESAs) could have made the tissue swelled and be responsible for a change in the mechanical properties of arteries.

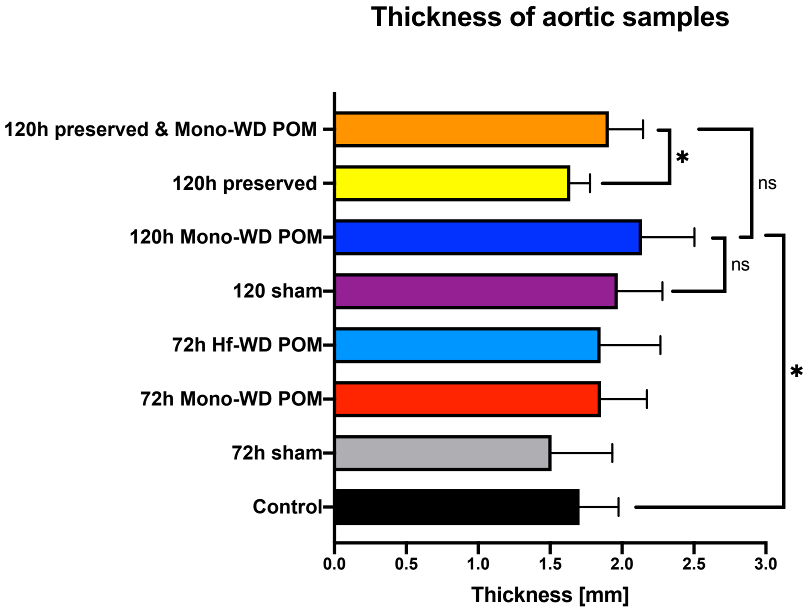

Figure 5.10: *Histogram representing the thickness of the samples corresponding to each condition, which has been measured just before testing. No significant difference is noticed between the control group and all the others, except for the 120h Mono-WD POM.*

Thickness variation is, generally, expected over the aortic length, but, no big differences are expected within one G segment. Each condition is constituted of samples coming from the 6 different aortas harvested, such that it should cancel out the variability among the different animals.

Moreover, groups 120h sham and 120h Mono-WD POM are constituted of samples coming from the exact same G segments. The same is true for the groups 120h preserved and 120h preserved & Mono-WD POM. Therefore, no differences in thickness should be seen if the solution does not affect the thickness of the arterial tissue.

Figure 5.10 represents a histogram with the mean thickness for each condition. First, by comparing the control group to all other conditions, no significant differences were seen, except with the group 120h Mono-WD POM. Then, by performing a comparison between the 120h sham and 120h Mono-WD POM, no significant differences were found. Therefore, Mono-WD POM should not influence the thickness of arterial tissue. However, between the group 120h preserved and the group 120h preserved & Mono-WD, a significant difference was seen ($P = 0.019$). The mean thickness of 120h preserved samples is 1.91 ± 0.24 mm and the mean thickness of the 120h preserved & Mono-WD is 1.64 ± 0.14 mm. In order to check whether the preservation solution changes the thickness of the tissue, the 120h preserved was compared to the 120h sham, and also the 120h preserved & Mono-WD POM to the 120h Mono-WD POM. A significant difference was obtain between the 120h sham group and the 120h preserved group, but no significant difference was seen between the 120h Mono-WD POM group and the 120h preserved & Mono-WD POM group. Therefore, it is difficult to give a clear conclusion whether or not the preservation solution can modify the thickness of the samples, more samples should be analysed.

Moreover, the curvature of the sample when deposited on the ground plate of the micro-laser could render the calculation of the thickness more imprecise, which could lead to a stronger variability among samples from the same segment. Different measuring techniques could be used to avoid imprecision errors due to the curvature of the sample, such as CE-CT. Furthermore, it is known that PBS also swells tissue. In order to draw a clear conclusion, the thickness of fresh samples (i.e. sample that are not frozen, neither immersed in PBS for a long time) should be assessed and compared to the control group, and more samples should be evaluated to compensate for the biological variability.

5.2.3 Effect of time

To assess the effect of time in the solution on the mechanical properties of arteries (i.e aging of samples), the mean stress-strain curves in the circumferential and axial directions were compared for three different conditions: the control group, the 72h sham and 120h sham group (Figure 5.11). There were no significant differences between the sham groups and the control group for the circumferential and axial direction. The standard deviation of the control samples was always less or equal to the standard deviation of the two sham groups. The Cauchy stress in the circumferential direction, σ_{11}, was higher than the one in the axial direction σ_{22}. Indeed, the mean value of the σ_{11} for the control group for the strain 15 %, is equal to 109 kPa whereas the mean value in the axial direction, σ_{22} is equal to 100 kPa. This is due to the orientation of the collagen and elastin fibers, both mostly aligned in the circumferential direction. This anisotropy effect becomes even more visible for the sham groups and will be further discussed in the section 5.2.7. Therefore, it was concluded that the time in the solution does not play a role on the mechanical properties of arteries.

It would be interesting, though, to obtain the stress-strain curve of fresh samples (i.e samples that would be tested directly after harvesting without a freezing step). Indeed, the effect of freezing on biological tissues is not well known. Slow freezing (i.e. sample deposited in a -80°C freezer), which has been used in this experiment, could have damage the sample as ice formed between the fibers. Indeed, the residual unfrozen medium forms channels of decreasing size and increasing solute concentration which makes cells shrink in osmotic response to this [73]. Sample expansion due to the formation of ice crystals could have changed the mechanical properties of arteries.

It can be concluded that, in this experiment the time in the solution does not influence the mechanical properties of arteries. Therefore, all differences seen with the stained samples come from the diffusion of the CESA in the tissue and are not due to tissue aging.

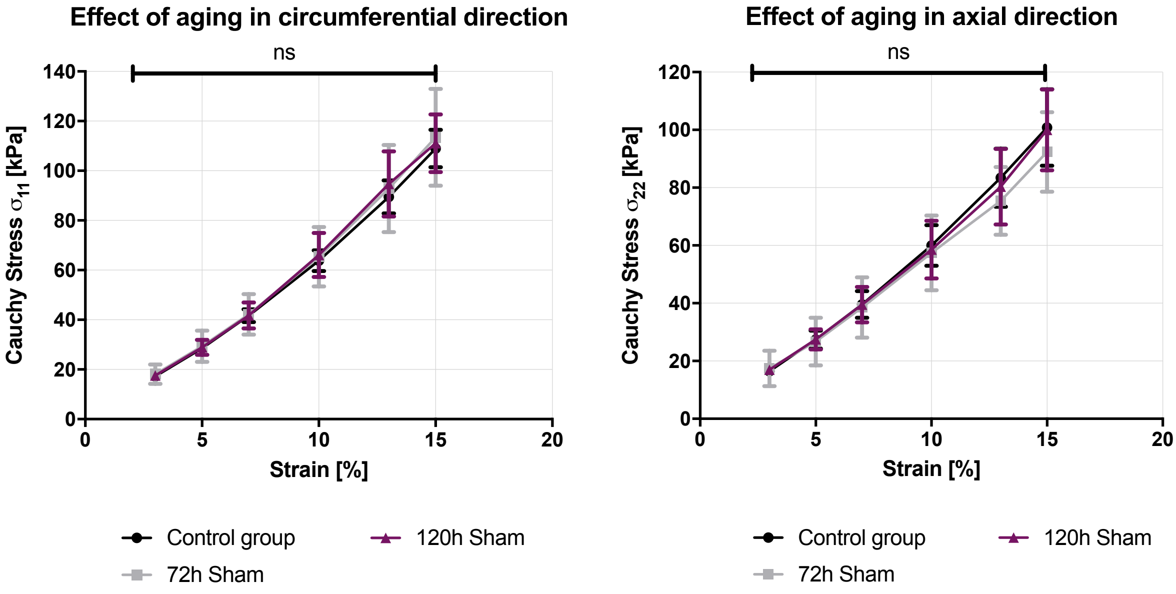

Figure 5.11: *The mean stress-strain curves are given in the circumferential and axial direction, of the control, 72h and 120h sham groups, with their respective standard deviation. No significant difference is obtained neither in the circumferential nor in the axial direction .*

5.2.4 Influence of the CESAs

By comparing the two 72h stained group (Hf-WD POM and Mono-WD POM), with the control group, the influence of the CESAs on the mechanical properties of arteries can be assessed, and both CESAs can be compared. Figure 5.12 shows significant differences between the stained groups and the control group for the circumferential direction. The same is true for Hf-WD POM in the axial direction. However, for the Mono-WD POM in the axial direction, a significant difference with the control group is only seen until 10% strain. Moreover, no significant differences were observed between the two stained groups for both directions.

The small difference for the 15% strain between the two CESAs could mean that at higher strain, the Mono-WD POM stiffens less the mechanical properties of arteries than Hf-WD POM, which could make the Mono-WD POM a more favorable CESA to use. Another reason to explain this difference, could come from the fact that during the experiment one or two needles of a rake were coming out of the sample before reaching the 20% load. This could have altered the forces sensed by the loading cells and given lower values for the Cauchy stresses. Indeed, stained samples had very little resistance for the needles. Nevertheless, this poor resistance to the needles was not present for the non-stained samples, for which the full experimental protocol have been performed. One way to determine if Mono-WD POM possesses a lower stiffening effect on arterial tissues, in comparison to Hf-WD POM, would be to use clamps instead of rakes. Rakes are often preferred, because they provide a uniform spacing, which restricts shear deformation of the sample. Though, in this case, it would be interesting to use clamps to avoid the sample from sliding away from the rakes, which would allow to asses the stress-strain curve at higher strain than the 15% strain.

The diffusion of the CESAs in arterial tissues leads to a stiffening effect of approximately 20-30 kPa for the 10% to 15% strain. This stiffening effect can come from the binding of the

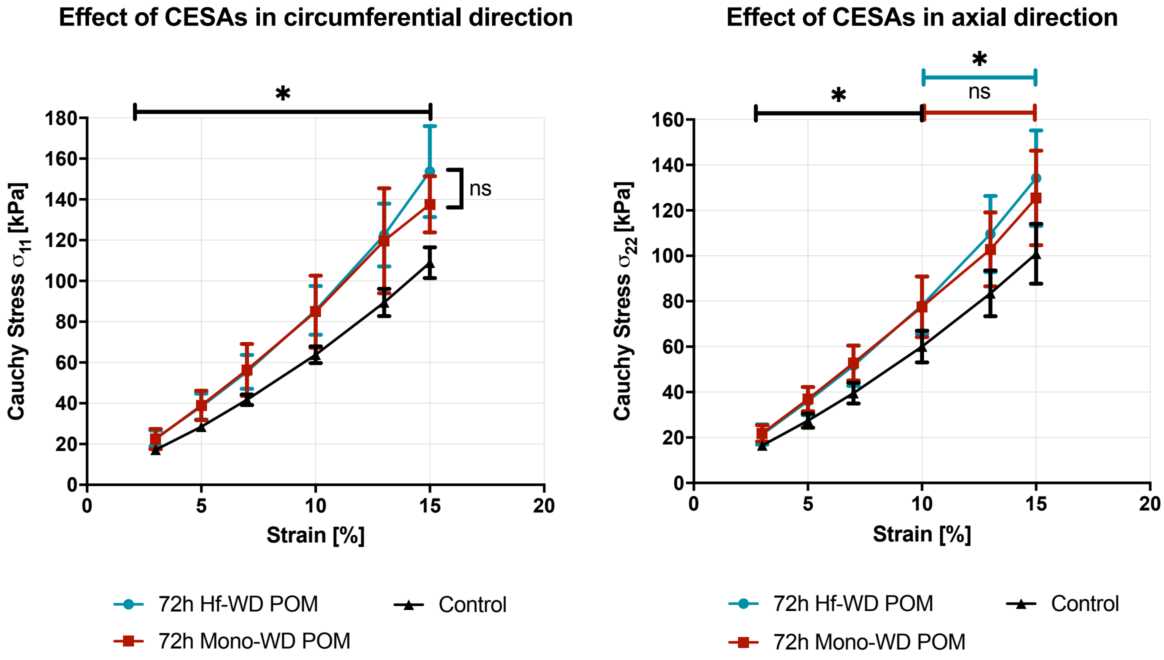

Figure 5.12: *The mean stress-strain curves are given in the circumferential and axial direction, of the control, 72h Hf-WD POM and 72h Mono-WD POM groups, with their respective standard deviation. A significant difference is obtained between the stained groups and the control one. However, no significant difference is noticed between the two stained groups.*

chemical compound to the proteins present in the tissue. Indeed, based on the CE-CT images of the rat thoracic aorta stained in Hf-WD POM, it was noticed that the chemical compounds had a strong affinity to the elastin lamellae as they appeared white. This binding could lead to a stiffening of the lamellae and explain the stiffer stress-strain curves. Moreover, no significant difference is seen between the two CESAs, both give the same stiffening effect as they possess similar binding mechanisms. However, at higher strain, Mono-WD POM might stiffen less the mechanical properties of arteries.

5.2.5 Effect of the staining time

The staining time is a crucial parameter for the good contrast properties when using CE-CT. The amount of time needed to obtain full diffusion in the tissue is dependent on the CESA used. By comparing the 72h stained Mono-WD POM condition with the 120h stained Mono-WD POM condition, it can be assessed whether the staining time influences the effect from the CESAs.

Figure 5.13 shows no significant differences between the two different staining times. An hypothesis that could explain this, would be that at 72h of staining, full diffusion of Mono-WD POM in the tissue has already been reached. Therefore, increasing the staining time even after the full diffusion of the CESA would not change the mechanical properties of arteries even more. Kerckhofs's team has recently assessed that Hf-WD POM and Mono-WD POM do not possess the same diffusion properties. For Hf-WD POM, 72h to 120h of staining is barely sufficient for obtaining good contrast properties when using CE-CT. However, only a day or two could be necessary to reach full diffusion of Mono-WD POM in the tissue, hence give good contrast properties. Therefore, this experiment should be repeated to assess the influence of the staining time with much shorter staining time for the Mono-WD POM CESA (e.g. 5h, 10h, 24h and 48h) and longer staining time than 72h for Hf-WD POM. This could confirm at which staining time full diffusion of the tissue has been reached taking as assumption, that once full diffusion has been reached the stiffening effect

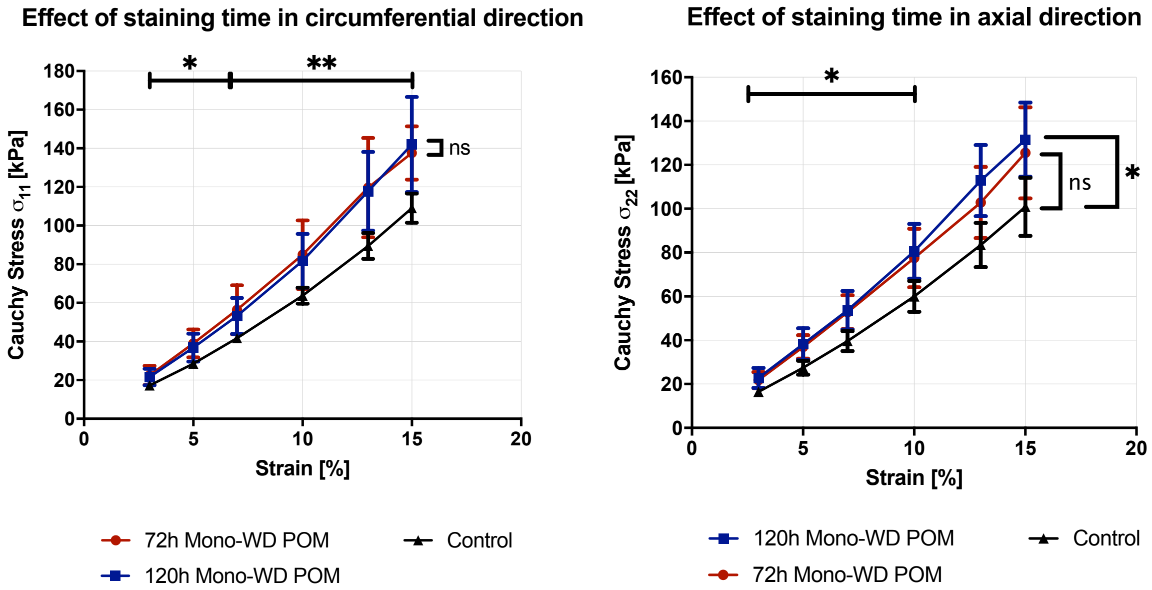

Figure 5.13: *The mean stress-strain curves are given in the circumferential and axial direction, of the control, 72h Mono-WD POM and 120h Mono-WD POM groups, with their respective standard deviation. A longer staining time does not lead to a significant difference as at 72h full diffusion of the CESA in the tissue has been reached. Moreover, both stained groups are significantly different from the control group, expect from strain 13% to 15% in the axial direction for the 72h Mono-WD POM group.*

of the stress-strain curve should not change.

The 120h Mono-WD POM group is significantly different from the control group for both directions, whereas for the 72h Mono-WD POM in the axial direction, this is only true until 10% strain .

5.2.6 Effect of the preservation solution

Figure 5.14 shows the stress-strain curves of three conditions: the 120h preserved, the 120h sham and the control group. For the axial direction, no significant difference between the three conditions were found. For the circumferential direction, however, a significant difference between the 120h preserved group and the control group was found (P = 0.018). For both directions, the 120h preserved and 120h sham conditions are not significantly different, and no significant differences are found between the 120h sham group and the control group. One reason for this could be that the high biological variability (i.e. large standard deviation) leads to a non-significant difference in the axial direction when using the multiple t-test analysis. Therefore, by performing this experiment again on a larger amount of samples, a clearer conclusion could be obtained, whether significant differences are found between the preserved group and the control group or not, in both directions.

Figure 5.15 represents the stress-strain curves for the 120h preserved & Mono-WD POM group, the 120h Mono-WD POM group and the control group. Depending on the direction of the Cauchy stress, two opposite effects were obtained. In the axial direction, the preservation solution seemed to lower the stiffening effect from the CESA. Nevertheless, this effect was not noticed in the circumferential direction, leading to a slightly stronger stiffening effect than the CESA alone. Indeed, in the circumferential direction, a significant difference was seen between the 120h preserved & Mono-WD POM group and the control group. However, in the axial direction, no significant differences between those two groups were observed. Moreover, no significant differences were obtained

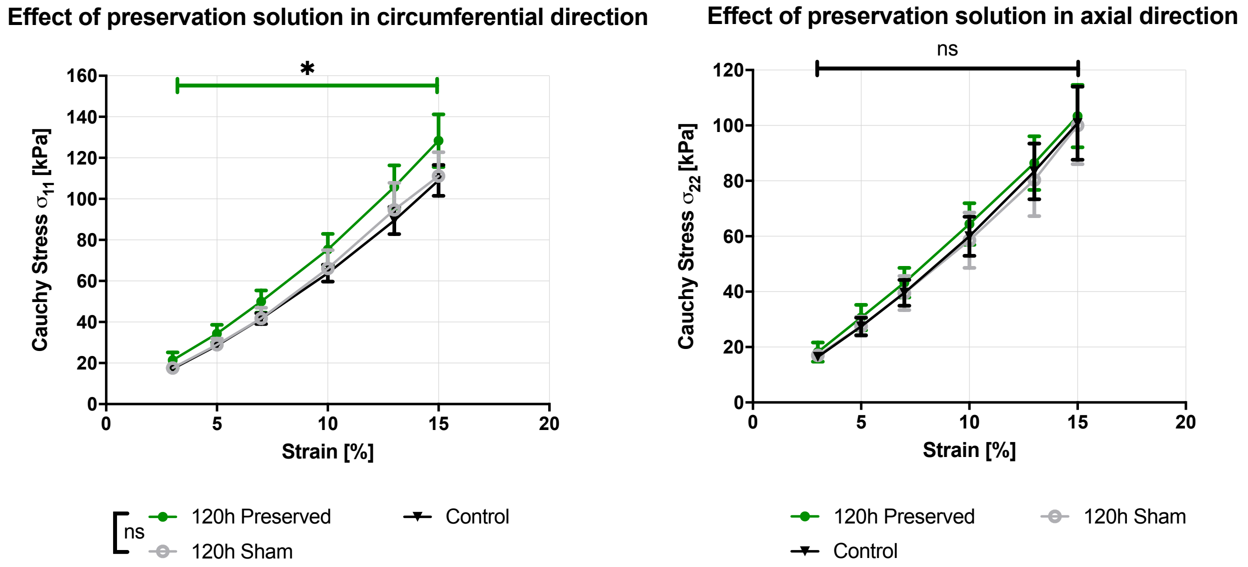

Figure 5.14: *The mean stress-strain curves are given in the circumferential and axial direction of the control, the 120h sham and the 120h preserved groups, with their respective standard deviation. In the circumferential direction, a significant difference between the control and the 120h preserved is obtain. However, in the axial direction, no significant difference is noticed.*

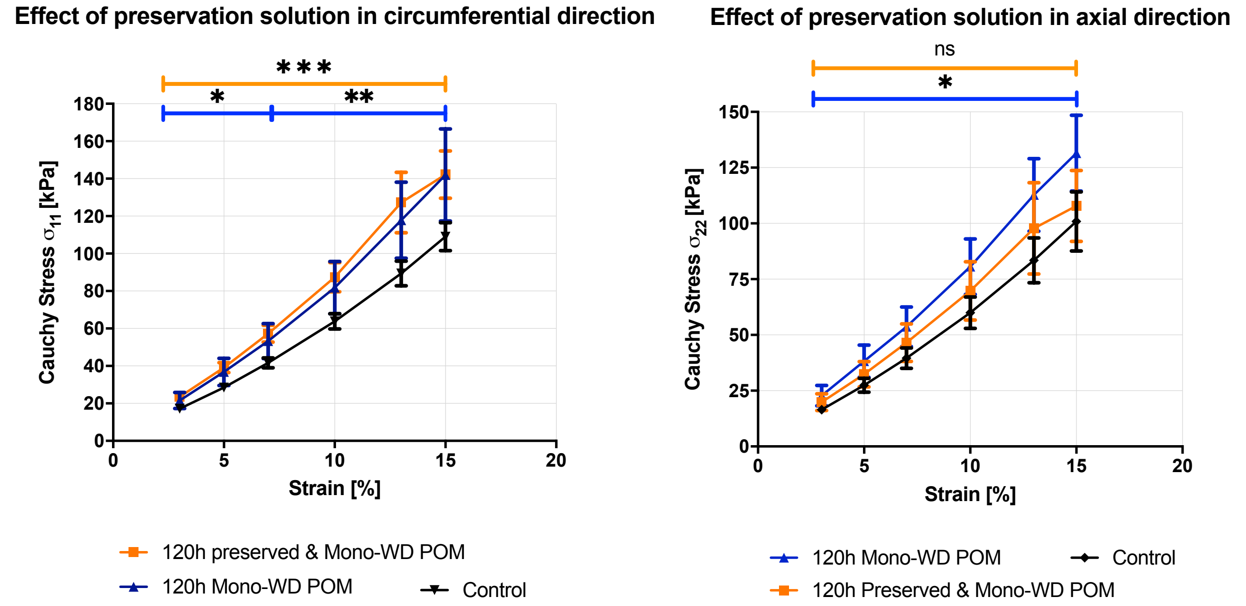

Figure 5.15: *The mean stress-strain curves are given in the circumferential and axial direction of the control, the 120h preserved & Mono-WD and the 120h Mono-WD groups, with their respective standard deviation. In the circumferential direction, a significant difference between the control and the 120h preserved & Mono-WD POM is obtain. However, in the axial direction, no significant difference is noticed.*

between the 120h Mono-WD POM and the 120h preserved & Mono-WD POM for both directions.

Furthermore, the relative random error of those two conditions can be calculated as the standard deviation divided by the mean value (Equation 5.5):

$$\epsilon_{r1} = \frac{\Delta\sigma_{11}}{\sigma_{11}}, \qquad \epsilon_{r2} = \frac{\Delta\sigma_{22}}{\sigma_{22}} \tag{5.5}$$

For the 120h Mono-WD POM group, a relative error of 18% and 13% was found for the circumferential and axial direction, respectively. The relative error for the 120h preserved & Mono-WD POM group was 9% and 15%, respectively, for the circumferential and axial direction. This larger relative error for the axial direction, compared to the circumferential direction, for the 120h preserved & Mono-WD POM group could potentially explain why two opposite effects were obtained in the two directions. Indeed, only 6 to 8 samples were tested under planar biaxial mode for each condition, whereas often in the literature over 50 samples are tested per condition in order to assess an effect [74]. If more samples are tested, the mean value of the Cauchy stresses obtained would be more accurate, so that maybe significant differences with the control group could be seen in both directions.

Another reason that could explain this difference is the sample demounting phenomena that occurs when samples are immersed in a CESA solution, leading to potential wrong reaction forces sensed by the loading cells and to a diminished displacement of speckles measured by the DIC camera, hence a potential incorrect strain field computed. This can alter the posterior calculation of the Cauchy stresses. The third reason is inherent of the Messphysik-Zwick/Roell planar biaxial testing machine. Indeed, the loading cells are designed to measure reaction forces ranging from 0.8 to 200 N, below 0.8N the accuracy of the load signal decreases drastically. By looking at Figure 5.16, the reaction forces sensed by the load cells are plotted.

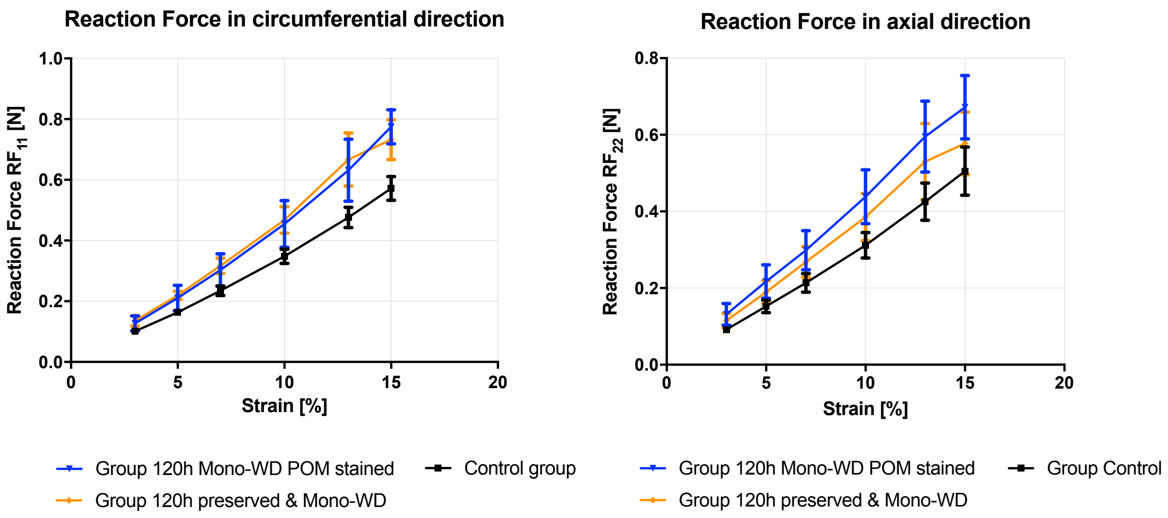

Figure 5.16: *The mean reaction forces are given in the circumferential and axial direction of the control, the 120h preserved & Mono-WD and the 120h Mono-WD groups, with their respective standard deviation. For almost all strains, the reaction forces are below the 0.8 N threshold. Threshold for which the accuracy of the load cells decreases.*

For the most part of the graphs, the reaction forces lie beneath the 0.8 N threshold. The fact that the load cells might not be sensitive enough for the arterial tissue is known by the FIBEr lab team. However, Zwick/Roell does not propose yet a smaller range of force detection. To obtain a clear conclusion on the effect of the preservation solution, the experiment should be repeated with more samples (e.g. 20 samples), and it should be assessed whether clamps could be better than rakes to avoid demounting of the samples.

5.2.7 Stiffness and anisotropy index

The stiffness of arterial samples can be calculated as the slope of their Cauchy stress-strain curves. Moreover, the Cauchy stress-strain curve is given for both the circumferential and axial direction, enabling the anisotropy index (AI) to be computed. This difference in directional response of the arterial tissue, i.e. the degree of anisotropy, can be calculated as the difference in stiffness between the two directions divided by the average stiffness [75]:

$$AI = \frac{E_{11} - E_{22}}{E_{avg}}, \text{ where } \quad E_{avg} = \frac{E_{11} + E_{22}}{2} \tag{5.6}$$

The anisotropy index and the stiffeness are interesting because both are influenced by the fibers organization [76]. They give an idea of the fiber orientation present in the tissue, which has become a crucial parameter in today arterial models. Indeed, for a long time and for simplicity, fibers were often considered to be aligned (i.e no anisotropy). However, now, several studies have shown that mechanical models that include the orientation distribution of fibers better describe the experimental mechanical behavior of arterial tissues [71, 76, 77, 78]. Moreover, knowing the stiffness of the control group enables comparison with the literature and other materials used in the biomedical field.

Table 5.3 gives the mean stiffness in both direction and the anisotropy index for the control group and all the other conditions. The control and sham groups have similar stiffness in both directions, confirming that time in solution does not influence the mechanical properties of arteries. The same is true for the three stained groups. However, for the 120h preserved and 120h preserved & Mono-WD POM, their stiffness vary a lot depending on the direction. In the axial direction, they possess similar stiffness as the control group, but in the circumferential direction, their stiffness is in between the control and the stained groups. This strong variation upon the direction is confirmed by their anisotropy index. Together with the 72h sham group, they possess the highest AI value.

Table 5.3: *Circumferential and axial stiffness is given, respectively, for all conditions, and the anisotropy index is also computed.*

Condition	Circ. stiffness E_{11} [MPa]	Axial stiffness E_{22} [MPa]	AI [-]
Control	0.77 ± 0.18	0.70 ± 0.28	0.09
72h Sham	0.80 ± 0.45	0.62 ± 0.40	0.25
120h Sham	0.80 ± 0.32	0.68 ± 0.34	0.16
72h Mono-WD POM	0.97 ± 0.64	0.85 ± 0.51	0.13
72h Hf-WD POM	1.07 ± 0.48	0.94 ± 0.47	0.13
120h Mono-WD POM	1.00 ± 0.54	0.91 ± 0.43	0.09
120h Preserved	0.89 ± 0.29	0.71 ± 0.25	0.22
120h Preserved & Mono-WD POM	1.03 ± 0.35	0.76 ± 0.43	0.30

By looking at the Table 5.4, it enables the comparison of the control group of this study with literature values on fresh porcine descending aortas (DA), i.e without a freezing step. H. de Beaufort made a review paper of 10 studies; 5 assessed the stiffness of porcine aortas and 5 other of humans aortas under planar biaxial testing [79]. The mean value of those 5 studies for the E_{11} and E_{22} stiffness of fresh porcine descending aorta is 0.46 MPa and 0.44 MPa, respectively. Those values are almost half the values of the control group in this study. This difference may arise from the freezing step and from the biological variability, as in this study 6-8 samples were only tested for each group. Moreover, these values can be compared to the one for human descending aortas. The stiffness of a human DA below 60 years old is not very different from the porcine DA. However, as a human ages, its arterial stiffness can drastically change and becomes much stiffer with a stronger anisotropy present. For the circumferential direction, the stiffness of human DA can triple over the course of his life. The challenge to design synthetic materials capable of delivering the right stiffness and the right anisotropy degree can be understood through this. Indeed, Table 5.4 gives the stiffness for dacron, a synthetic material used clinically for bypass surgery to replace an obstructed artery. It is composed of polyethylene terephthalate fibers [84]. The stiffness values in both directions have been assesed by A. Coirbay [82], and a very strong anisotropy and a very high stiffness is noticed. It can be 5 to 10 times more stiff than a human aorta. Moreover, the same observation can be done with poly-L-lactic acid (PLLA), also a synthetic material used in vascular graft, which possess much higher stiffness than the human DA. Unfortunately, those compliance mismatches are the first reason of vascular graft failure. Therefore, synthetic materials should be better designed in order to mimic more closely the stiffness of human arteries and their degree of anisotropy.

Table 5.4: *Comparison with the literature values and with other types of materials used in the biomedical field.*

Condition	Stiffness E_{11} [MPa]	Stiffness E_{22} [MPa]	AI
Fresh porcine DA [79]	0.46 ± 0.03	0.44 ± 0.01	0.04
Human DA (< 60 years) [80]	1.04 ± 0.70	1.24 ± 0.76	(-) 0.18
Human DA (>60 years) [80, 81]	3.15 ± 3.31	1.17 ± 0.31	0.92
Dacron vascular graft [82]	13.65	5.75	0.81
PLLA vascular graft [83]	6.24 ± 1.69	29.54 ± 5.85	(-) 1.3

5.2.8 GOH material model

Once the experimental stresses have been calculated, the in-house developped Matlab code proceed to a parameter fitting procedure in order to find the best approximated values of the Gasser-Odgen-Holzapfel (GOH) model. The GOH material model is composed of 5 parameters. Three of them are particularly interesting to discuss. Indeed, k_1 is a stress-like parameter related to the fiber stiffness, κ is related to the dispersion of fibers with values ranging from 0, i.e. no dispersion of fibers, to $\frac{1}{3}$, corresponding to full dispersion, and α is defined as the angle between the mean collagen fiber direction and the circumferential direction, where 0 represents the circumferential direction and π the axial direction. Moreover, the parameter fitting procedure gives the normalized root mean square error (NRMSE), which represents a measure of the goodness of the fit.

Figure 5.17 represents a histogram with the values for the three mentioned parameters of the GOH model for 5 different conditions. Those 5 different conditions have been chosen because they correspond to the 5 effects analysed in this study. No significant differences were obtained for all parameters and for all conditions, except for the parameter κ of the group 120h preserved & Mono-WD POM. Moreover, all groups posses a relatively small NRMSE, which is around 0.4, except for the 120h preserved & Mono-WD POM, which possess a NRMSE above 1. This can probably explain why the parameter κ of this group is significantly different than the κ of the other groups.

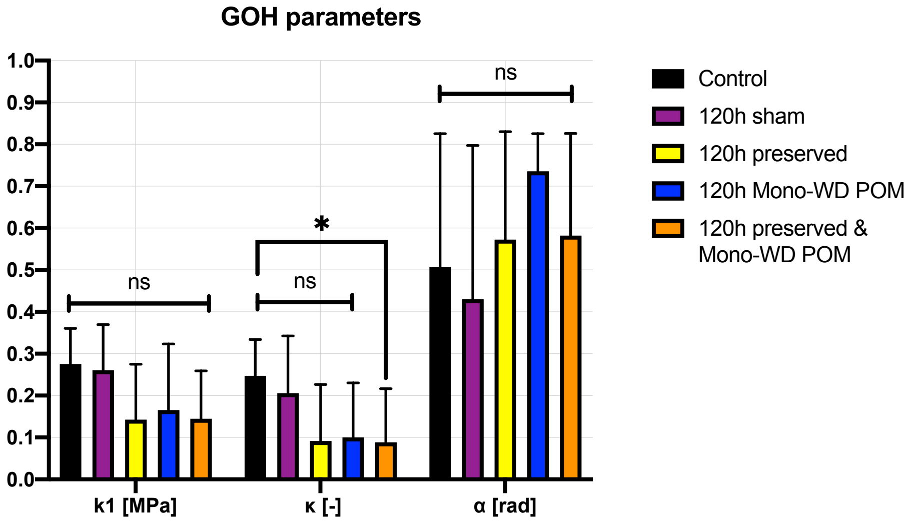

Figure 5.17: *Three of the Gasser-Odgen-Holzapfel parameters are given. They respresent, respectively, the stiffness of the fibers, the dispersion of the fibers and the angle between the mean direction of the fibers and the circumferential direction. No significant differences are obtained for all groups, except for κ for the 120h preserved & Mono-WD POM group.*

Despite no significant differences, it is possible to compare the mean values, and some visual differences can be seen among the 5 different conditions. Surprisingly, the k_1 value is lower for the stained and the preserved groups than of the sham and the control group. As k_1 is related to the stiffness of the fibers and is expressed in MPa, it would be expected that for the conditions, that posses a higher stiffness, would possess a higher k_1 value. For the κ parameter, lower values of fiber dispersion were found for the stained and preserved groups. This would theoretically mean that the fibers orientation changes upon diffusion of a CESA or of the preservation solution. However, this seems unrealistic. Therefore, another possible explanation could be that the model does catch a difference among the stress-strain curves of the stained and the preserved samples compare to the control samples, but as it is a parameter fitting procedure, the model tries to find the best values to fit the experimental curves and it interprets this as a change in the dispersion of fibers. If fibers are aligned in a single direction with little dispersion, the stiffness increases. The GOH model was designed to model arterial tissue, but maybe not arterial tissue that has been stained. Therefore, more parameters should be included to have a better idea of what is happening when tissue are preserved or stained.

Finally, the α parameter can be discussed. A higher mean value is seen for the 120h Mono-WD POM group, and for the other groups similar values, close to 0.5-0.6 rad, are obtained. A more obtuse angle means that the mean fiber orientation tend to align more to the axial direction than the circumferential direction. However, the values of α remains quite small, which is logic as it is known that collagen fibers are mostly aligned in the circumferential direction [85], hence α values closer to 0 than to π are expected, which is the case in this study.

5.3 Conclusion

We have found that the aging of the samples after a freezing step had no influences on the mechanical properties of arteries. However, the two CESAs used, Hf-WD POM and Mono-WD POM, both contributed to a stiffening effect of the stress-strain curves of 20 to 30 kPa for the 15% strain. No significant difference has been seen between the two CESAs, making them both suitable for 4D CE-CT. A longer staining time for Mono-WD POM did not influence the mechanical properties of arteries. Regarding the effect of the preservation solution, no clear conclusion could be made due to the demounting of the samples, the high relative random errors and the loading cells sensitivity. It should, therefore, be further studied. We have also discussed the challenge of having an accurate material model that fully grasps the mechanical behavior of arteries. For 4D CE-CT, it should be keept in mind that the mechanical behavior of stained arterial tissue is stiffer than of the frozen arterial tissue, and the frozen arterial tissue itself might also be stiffer than the fresh tissue. However, the microstructure should not be affected by the diffusion of the CESA and the preservation solution, as no significant differences in the thickness of the samples were obtained, enabling the characterization of the relationship between the mechanical behavior of arteries and their microstructure, thanks to 4D CE-CT.

6

General conclusion and further perspectives

The goals of this master thesis were to first create an image analysis protocol to analyse the microstructure of arteries in details, and second to assess whether different CESAs influenced the mechanical properties of arteries, both with the aim to assess the feasibility of 4D CE-CT testing of arterial tissues. For the second goal, several different conditions have been tested using planar biaxial testing, and the effect of the CESA staining, the staining time and of a preservation solution on the mechanical properties have been determined.

With regards to the image analysis protocol, we concluded that, although this thesis allowed to set up the protocol, multiple samples of different rat thoracic aortas should be assessed. Moreover, not only Hf-WD POM should be used for staining, but also Mono-WD POM, and the staining capacity of both should be compared. Indeed, as it is expected that a shorter staining time is required for Mono WD-POM, compared to Hf-WD POM, to reach full diffusion of the CESA in the tissue, several samples stained in Mono-WD POM with different staining time should be analysed in order to assess the ideal staining time. Also the affinity of Mono-WD POM for the elastin lamellae should be assessed. Good constrast properties enables to characterize specifically the lamellae found in the media layer, which is of great interest for a better understanding of their role in the mechanical behavior of arteries. Moreover, this could be implemented in computer models of arteries to take into account both collagen and elastin fibers. Another intermediate step before performing the 4D CE-CT could be to scan the stained samples after being tested mechanically and to compare it with non-tested samples. This would allow to notice if differences exists after a planar biaxial test.

Concerning the mechanical testing of arteries, the experiments done in this study, could be repeated with clamps instead of rakes in order to avoid the demounting of the stained samples. This would allow to obtain experimental results above the 15% strain. Moreover, all conditions should be further studied with a larger amount of samples in order to have a clearer view of their effect on the mechanical properties of arteries. The mechanical properties of fresh samples (i.e. non-frozen) should be assessed and compared with the control group.

Finally, general research on different CESAs should be continued, maybe different CESAs might stiffen less the mechanical properties of arteries. However, if we cannot find a CESA that has almost no stiffening effect on the mechanical properties of arteries, the stiffening effect seen in the stress-strain curves by those CESAs should be assessed in greater detail. Indeed, if we know exactly by how much a CESA stiffens the mechanical properties of arteries, we could retrieve the expected stress-strain curve of a fresh sample. This could be implemented in a new model that takes into account the stiffening effect from the CESA used and retrieves the expected stress-strain curves.

Challenges remain before fully characterizing the mechanical behavior and its relationship with the microstructural properties of arteries. 4D CE-CT would, therefore, bring insight on this relationship that links the mechanical properties with the microstructure, and allows for a better design of a vascular graft, which purpose is to improve the life of the patients suffering from cardiovascular diseases. We are convinced that the present thesis brought an incremental contribution to the achievement of 4D CE-CT, and will pave the way for additional research on the matter by offering ideas for the next steps.

Appendices

A

Arterial compliance measurement

Calculating the arterial compliance requires the measurement of the vessel diameter, the distension and wall thickness which can be difficult to obtain. Therefore, J. Joseph and his team developped a single ultrasound transducer element for the evaluation of arterial compliance *in-vivo* [14]. Figure A.1 shows the working principle of their device. It is based on a dynamic threshold algorithm to identify artery walls and it uses a correlation based tracking technique to estimate arterial distension.

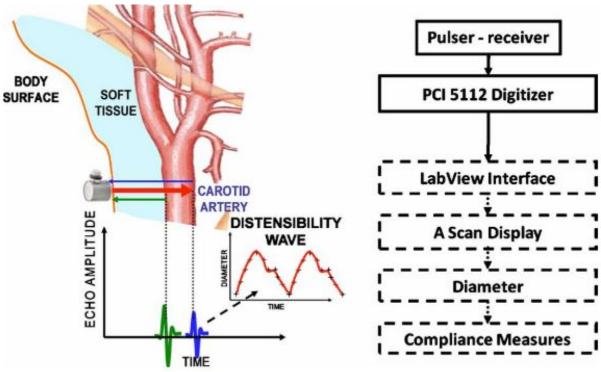

Figure A.1: *Noninvasive measurement of arterial compliance based on a single ultrasound transducer element [14].*

The single element ultrasound transducer is placed on the neck of the subject about 2 cm below the carotid bulb. The working principle of the transducer is based on the pulse echo modality using the commercial pulse receiver (Model 5800 PR, Olympus NDT) where it sends out ultrasound pulses into the body at a frequency of 5 MHz. The sound pulses get reflected from the near and far walls of the carotid artery and the echoes comes back to the transducer. With this, they estimated the diameter of the artery in terms of the difference between the times of arrival of the two echoes Δt multiplied by the sound velocity v as follow:

$$d = \frac{1}{2} \times v \times \Delta t \tag{A.1}$$

The transducer is such that only the echoes of the beam passing normal to both near and far walls are received. Indeed the narrow beam width (3 dB half angle of 1.3°) of the transducer ensures that only strong echoes are received as any portion of the beam not passing perpendicularly to the artery will tend to get reflected away from the transducer due to the circular geometry of the artery. The received echoes are then digitized using a PCI-5112 digitizer card (National Instruments) and are further process thanks to LabView® software.

The distension of the artery is obtained by continuously keeping track of the movement of the

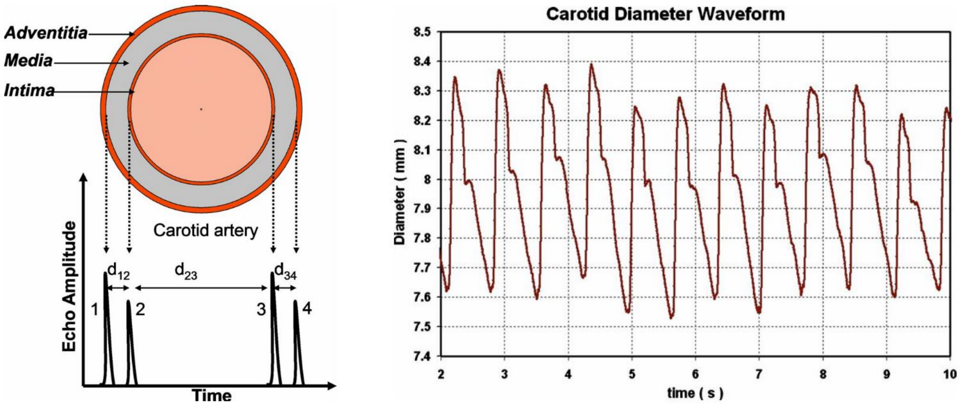

Figure A.2: *On the left, conceptual sketch of the carotid artery and expected echo peaks. On the right, the carotid diameter waveform graph calculated via the echo peaks [14].*

echoes coming from the walls of the artery and can then be plotted as the distensibility waveform. The numerator of the compliance equation A.2, ΔD, is obtained by calculating the peak to peak distension in the distensibility waveform graph as shown in Figure A.2. Finally, in order to obtain the denominator of the compliance equation, ΔP, accurate measurement of the carotid artery blood pressure is necessary. However, it is a very difficult task as only invasive techniques exist and are not not suitable for clinical studies [86]. The brachial artery pressure can thus be used as a substitute for the carotid pressure and can be measured using an automatic blood pressure monitor (HEM-7101, OMRON) [14]. The blood pressure variation over a cardiac cycle is then calculated and can be fed in equation A.2.

$$C = \frac{\Delta D}{\Delta P} \tag{A.2}$$

Table A.1 gives the arterial compliance estimated using this technique for three different volunteers.

Volunteer	Age	Mean distension (μm)	Compliance ($\mu m/mmHg$)
A	24	440	11.0
B	30	712	17.8
C	32	294	7.34

Table A.1: *Arterial compliance estimated for three different volunteers [14].*

They reported that their instrument could measure arterial distension with a precision better than 5% and with an accuracy of 1%. This technique allows non-invasive, in-vivo and fast arterial compliance measurement, and is especially used as a test to detect and predict the risk of cardiovascular disease.

B

The GOH model

The Gasser-Ogden-Holzapfel (GOH) material model is a structural constitutive model that describes an incompressible, fiber-reinforced and anisotropic material. It was designed to model arterial tissues. It accounts for the dispersion of two fiber families, namely collagen I and collagen II [72, 87]. The GOH model defines a strain energy density function (SEDF) Ψ that contains two terms: an isotropic one and an anisotropic term. They correspond, respectively, to the matrix material and to the collagen fiber families. The SEDF is expressed as follow [71]:

$$\Psi = C_{10}(I_1 - 3) + \sum_{i=4,6} \frac{k_1}{2k_2}[e^{k_2(\kappa I_1+(1-3\kappa)I_i-1)^2} - 1] \tag{B.1}$$

where $C_{10} > 0$ and $k_1 > 0$ are stress-like parameters, related to the matrix and to the fiber stiffness, respectively. $k_2 > 0$ is a dimensionless parameter and $\kappa \in [0; \frac{1}{3}]$ is a parameter related to the dispersion of the fibers, with 0 being a lower limit and corresponding to no fiber dispersion, and with $\frac{1}{3}$ being the upper limit and corresponding to full dispersion of fibres. I_1 is the first invariant of the right Cauchy Green tensor C and I_4 & I_6 are invariants of C related to the stretch in the mean direction of each fiber family. And C is defined as a function of the deformation gradient:

$$\mathbf{C} = \mathbf{F^T F} \tag{B.2}$$

$$I_1 = tr(\mathbf{C}) \tag{B.3}$$

$$I_4 = \mathbf{m}.(\mathbf{Cm}) \tag{B.4}$$

$$I_6 = \mathbf{n}.(\mathbf{Cn}) \tag{B.5}$$

$\mathbf{m}$ & $\mathbf{n}$ are the fiber vectors, and represent the mean fiber direction as a function of an angle α defined as the angle between the mean fiber direction and the circumferential direction.

By applying a parameter fitting approach based on the experimental Cauchy stress $\boldsymbol{\sigma}$, it is possible to determine the five GOH material model parameters values: C_{10}, k_1, k_2, α and κ. Indeed, the link between the experimental Cauchy stress expression and the SEDF function is given by:

$$\boldsymbol{\sigma} = J^{-1}\mathbf{PF^T} \tag{B.6}$$

$$\mathbf{P} = -p\mathbf{F^{-T}} + \frac{\delta\Psi}{\delta\mathbf{F}} \tag{B.7}$$

where J is the jacobian calculates as the determinant of the deformation gradient matrix ($J = det(\mathbf{F})$), $\mathbf{F}$ is the deformation gradient and $\mathbf{P}$ is the first Piola Kirchhoff stress that is expressed as a function of Ψ and of the hydrostatic pressure p. Table B.1 shows the lower and upper limit values for these five GOH material model parameters.

Table B.1: *Upper and lower boundaries for the parameters of the GOH model.*

Boundaries	C_{10} (MPa)	k_1 (MPa)	k_2	κ	α (RAD)
Lower	10^{-4}	0	10^{-4}	0	0
Upper	1	10	100	1/3	π

C

CESAs and preservation solution: protocol

Mono-WD POM solution preparation

Mono-WD POM is an in-house 3.5% prepared solution. The Mono-WD POM powder is dissolved in PBS with LiCl to improve the diffusion properties of the CESA in the tissue. The solution was prepared the same day of the samples immersion to avoid any sedimentation of the powder. The volume of the CESA solution needed depends on the number of samples that needs to be immersed. Every sample is immersed in its own eppendorf tube, and per eppendorf tube 2.5 ml of solution is required and 10% extra is added to account for the imprecision and losses by the laboratory pipettes .

For 8 samples, a volume of 22 ml was required:

$$8_{\text{samples}} \times 2.5ml = 20ml + 10\% \times 20ml = 22ml \tag{C.1}$$

The concentration of the Mono-WD POM powder is of 35mg/ml and came from batch 2. Mentioning the batch number used, ensures that if the experiment is repeated with the same batch the differences that might arise from different preparations of the CESA powder can be ruled out. For 22 ml of volume, 0.770 g of Mono-WD POM was needed. The concentration of Lithium chloride (LiCl) is equal to 3mg/ml and for a volume of 22ml, 0.066g was required. The powder were weighed using a KERN balance that has a precision of 0.0001g. Using a plastic spoon, 0.769g of Mono-WD POM was deposited in a falcon flask. Then, 0.068g of LiCl were deposited in the same falcon flask. It corresponds to approximately 2% of error. Then, 22ml of PBS were added in the falcon flask. The solution had to be shaken until no powder was visible.

Once the solution was prepared, 2.5 ml of the solution was poured in every eppendorf tube. Then, the sample was deposited in the eppendorf tube and the whole was placed on a shaker plate for the amount of time required by the condition (i.e. 72h or 120h).

Hf-WD POM solution preparation

The preparation of the Hf-WD POM was the same as the one of the Mono-WD POM, except for the LiCl powder, which was not added. Hf-WD POM is an in-house 3.5% prepared solution as well. The Hf-WD POM powder (batch 8) was dissolved in PBS. The concentration of the Hf-WD POM is 35mg/ml so that the same amount needed to be weighed. The preparation was prepared by Greet Kerckhofs and the amount actually weighed are not known.

Preservation solution preparation

The reagents to prepare the preservation solution are as followed [51]:

- **EDTA**: ethylenedinitrilotetraacetic acid disodium salt dihydrate 5mM, (Titriplex III), Merck - Millipore, CASn°: 6381-92-6, catn°: 1.08418.5000

- **Benzamidine hydrochloride powder**: 5mM, Sigma, CASn°: 1670-14-0, catn°: 434760-5G
- **Antibiotic-Antimycotic**: 100× Gibco - Life Technologies, catn° 15240-062 100 ml

A solution of 40 ml have been prepared by Sarah Vangrunderbeeck, the chemist of Kerchkofs team at Gasthuisberg laboratory. Table C.1 gives the initial concentration and the amounts needed for all reagents, and the amounts actually weighed.

Table C.1: *The reagents needed for the preparation of the preservation solution are given with their concentration. The amount needed and amount actually weighed are also given.*

Reagent	Concentration [g/mol]	Amount needed [mg]	Amount weighed [mg]
EDTA	372.24	74.4	74.41
Benzamidine HCl	156.61	31.3	31.34
Antibiotic-Antimycotic	100×	2ml	2ml

The protocol is as follow: 74.4 mg of EDTA and 31.3 mg of benzamidine HCl were weighed and added to a new flask. Next, 20 mL of PBS was added. The solution was shaken until the compounds are completely dissolved. Next, 2.0mL of the 100x stock solution of Anti-Anti was added, and the solution was diluted with PBS until 40 mL were reached (38 mL of PBS was added).

Once the solution is prepared, 2.5 ml was poured in every eppendorf tube. Then, the sample was deposited in the eppendorf tube and the whole was put on a shaker plate for the amount of time required by the condition (i.e. 120h).

To prepare the preservation solution with the Mono-WD POM, the already prepared preservation solution was used and the Mono-WD powder and the LiCl powder were added to this solution in order to keep a 3.5% solution. Therefore, to prepare 20ml of preservation solution with Mono-WD POM, 0.700g of Mono-WD POM was weighed and poured in a new flask. In the same flask, 0.06g of LiCl was added. Then, 20ml of the already made preservation solution were deposited in the flask. It is important to mix the solution for at least 5 min, in order to obtain good dissolution and avoid sedimentation.

Bibliography

[1] *Anatomy and Physiology II*, module 4: The cardiovascular system: Blood vessels and circulation. OER services, `https://courses.lumenlearning.com/suny-ap2/chapter/structure-and-function-of-blood-vessels/` (Accessed April 14^{th} 2020).

[2] *Drawing veins structure.* OER services, `https://ya-webdesign.com/image/drawing-veins-structure/1056804.html` (Accessed April 14^{th} 2020).

[3] *Les laboratoires Servier, SAS.* `https://smart.servier.com/smart_image/aorta/` (Accessed March 3^{rd} 2020).

[4] Charanpreet Singh, Cynthia Wong, and Xungai Wang. Medical Textiles as Vascular Implants and Their Success to Mimic Natural Arteries. Journal of Functional Biomaterials, 6(3):500–525, 2015.

[5] G. A. Holzapfel. Biomechanics in soft tissue. Handbook of material behavior, (7):149–154, 2001.

[6] Ayllon Bejar. Arterial grafts : in depth characterisation of structure andmechanical properties. Ecole polytechnique de Louvain, Université catholique de Louvain, Prom. : Kerckhofs, Greet ; Lacroix, Valérie., 2019.

[7] Walton et al. Morphological characterisation of unstained and intact tissue micro-architecture by X-ray computed micro- and nano-tomography. Scientific Reports, 5(March):1–14, 2015.

[8] Michael D Bentley. Review – 3D Micro CT Imaging of Renal Micro-Structural Changes. ResearchGate, (February), 2006.

[9] Katrien De Clercq, Eleonora Persoons, Tina Napso, Catherine Luyten, Tatjana N. Parac-Vogt, Amanda N. Sferruzzi-Perri, Greet Kerckhofs, and Joris Vriens. High-resolution contrast-enhanced microCT reveals the true three-dimensional morphology of the murine placenta. Proceedings of the National Academy of Sciences of the United States of America, 116(28):13927–13936, 2019.

[10] Butters et al. Optimal iodine staining of cardiac tissue for X-ray computed tomography. PLoS ONE, 9(8):1–6, 2014.

[11] Fehervary Heleen. Planar biaxial testing of soft biological tissues. KU Leuven, 2018.

[12] Pan et al. Two-dimensional digital image correlation for in-plane displacement and strain measurement: A review. Measurement Science and Technology, 20(6), 2009.

[13] Heleen Fehervary, Marija Smoljkic, Jos Vander Sloten, and Nele Famaey. Planar biaxial testing of soft biological tissue using rakes: A critical analysis of protocol and fitting process. Journal of the Mechanical Behavior of Biomedical Materials, 61, 01 2016.

[14] Jayaraj Joseph and V. Jayashankar. A virtual instrument for automated measurement of arterial compliance. Journal of Medical Devices, Transactions of the ASME, 4(4):1–13, 2010.

[15] Sébastien De Bournonville, Sarah Vangrunderbeeck, Hong Giang, T Ly, Carla Geeroms, Wim M De Borggraeve, Tatjana N Parac-vogt, and Greet Kerckhofs. Exploring polyoxometalates as non-destructive staining agents for contrast-enhanced microfocus computed tomography of biological tissues. (xxxx), 2020.

[16] Bruker Micro-CT. Morphometric parameters measured by Skyscan $^{\mathrm{TM}}$ CT - analyser software . pages 1–49.

[17] *Cardiovascular diseases (CVDs).* `https://www.who.int/news-room/fact-sheets/detail/cardiovascular-diseases-(cvds)` (Accessed October 30^{th} 2019).

[18] & Santulli G. Shu J. Update on peripheral artery disease: Epidemiology and evidence-based facts. Atherosclerosis, page 379–381, 2018.

[19] Dina S. et al. Cardiovascular tissue engineering: State of the art. Pathologie Biologie, 53(10):599–612, 2005.

[20] Chen Huan and Ghassan S. Kassab. Microstructure-based biomechanics of coronary arteries in health and disease. Journal of Biomechanics, 2016.

[21] G. Holzapfel. Collagen in Arterial Walls: Biomechanical Aspects. In: FRATZL, P. (ed.) Collagen Structure and Mechanics. Collagen: Structure and Mechanics, Springer V:Heidelberg, Germany, 2008.

[22] C Velican and Doina Velican. Study of Coronary Intimal Thickening. 56:331–344, 1985.

[23] *Circulatory System*, histology guide of the university of leeds. `https://www.histology.leeds.ac.uk/circulatory/arteries.php`. (Accessed August 10^th 2020).

[24] Raimund Erbel. Aortic dimensions and the risk of dissection. pages 137–142, 2006.

[25] Robert E. Shadwick. Mechanical design in arteries. Journal of Experimental Biology, 202(23):3305–3313, 1999.

[26] *Arterial Physiology*, pathway medicine. `http://www.pathwaymedicine.org/arterial-physiology`. (Accessed December 12^th 2019).

[27] Robert S Reneman and Arnold P G Hoeks. Noninvasive vascular ultrasound : An asset in vascular medicine. 45:27–35, 2000.

[28] Carmine Cardillo, Crescence M. Kilcoyne, Arshed A. Quyyumi, Richard O. Cannon, and Julio A. Panza. Selective defect in nitric oxide synthesis may explain the impaired endothelium-dependent vasodilation in patients with essential hypertension. Circulation, 97(9):851–856, 1998.

[29] Fleming I Busse R. Endothelial Dysfunction in Atherosclerosis. J Vasc Res, 97(9):181–194, 1996.

[30] Janssen MJ Donker AJ Stehouwer CD van Guldener C, Lambert J. Endothelium-dependent vasodilatation and distensibility of large arteries in chronic haemodialysis patients. Nephrol Dial Transplant, 1997.

[31] The mechanical behavior of vascular grafts: A review. Journal of Biomaterials Applications, 15(3):241–278, 2001.

[32] *Histological Techniques*, university of columbia. Center for Teaching and Learning, `https://histologylab.ctl.columbia.edu/histological_techniques/` (Accessed April 19^{th} 2020).

[33] *Micro computed tomography (micro-CT)*, bruker. `https://www.bruker.com/products/microtomography/micro-ct-for-sample-scanning/x-ray-micro-ct-microtomography.html` (Accessed May 1^{st} 2020).

[34] *How does a micro-CT scanner work?*, micro phtonics inc. `https://www.microphotonics.com/how-does-a-microct-scanner-work/` (Accessed May 1^{st} 2020).

[35] De Bournonville, Sarah Vangrunderbeeck, and Greet Kerckhofs. Contrast-Enhanced MicroCT for Virtual 3D Anatomical Pathology of Biological Tissues : A Literature Review. 2019.

[36] Mareike Töpperwien, Andrea Markus, Frauke Alves, and Tim Salditt. Contrast enhancement for visualizing neuronal cytoarchitecture by propagation-based x-ray phase-contrast tomography. NeuroImage, 199(May):70–80, 2019.

[37] Greet Kerckhofs, Steve Stegen, Nick van Gastel, Annelies Sap, Guillaume Falgayrac, Guillaume Penel, Marjorie Durand, Frank P. Luyten, Liesbet Geris, Katleen Vandamme, Tatjana Parac-Vogt, and Geert Carmeliet. Simultaneous three-dimensional visualization of mineralized and soft skeletal tissues by a novel microCT contrast agent with polyoxometalate structure. Biomaterials, 159:1–12, 2018.

[38] B.A. Lakin, D.J. Grasso, S.S. Shah, R.C. Stewart, P.N. Bansal, J.D. Freedman, M.W. Grinstaff, and B.D. Snyder. Cationic agent contrast-enhanced computed tomography imaging of cartilage correlates with the compressive modulus and coefficient of friction. Osteoarthritis and Cartilage, 21(1):60 – 68, 2013.

[39] Erica L Scheller, Nancy Troiano, Joshua N Vanhoutan, Mary A Bouxsein, Jackie A Fretz, Yougen Xi, Tracy Nelson, Griffin Katz, Ryan Berry, Christopher D Church, Casey R Doucette, Matthew S Rodeheffer, Ormond A Macdougald, Clifford J Rosen, and Mark C Horowitz. Use of osmium tetroxide staining with microcomputerized tomography to visualize and quantify bone marrow adipose tissue in vivo. Methods in enzymology, 537:123—139, 2014.

[40] Gina Delia Roque-torres. Micro-computed Tomography (micro-CT) in Medicine and Engineering. 2020.

[41] Brian D Metscher. MicroCT for comparative morphology : simple staining methods allow high-contrast 3D imaging of diverse non-mineralized animal tissues. 14, 2009.

[42] Stephen P. Dibartola. Fluid, Electrolyte, and Acid-Base Disorders in Small Animal Practice. W.B. Saunders, Saint Louis, third edition edition, 2006.

[43] Concentration-dependent specimen shrinkage in iodine-enhanced microCT. Journal of Anatomy, 223(2):185–193, 2013.

[44] R A Macrae, K Miller, and B J Doyle. Methods in Mechanical Testing of Arterial Tissue : A Review. Strain, pages 380–399, 2016.

[45] Bing Pan, Huimin Xie, Zhaoyang Wang, Kemao Qian, and Zhiyong Wang. Study on subset size selection in digital image correlation for speckle patterns. Optics Express, 16(10):7037, 2008.

[46] Bing et al Pan. Full-field strain measurement using a two- dimensional savitzky-golay digital differentiator in digital image correlation. Elsevier, 2009.

[47] Bing Pan, Anand Asundi, Huimin Xie, and Jianxin Gao. Digital image correlation using iterative least squares and pointwise least squares for displacement field and strain field measurements. 47:865–874, 2009.

[48] Sudhanshu S Singh and Nikhilesh Chawla. 3D/4D X-Ray Microtomography: Probing the Mechanical Behavior of Materials. pages 2013–2033, 2016.

[49] Clément Jailin, Amine Bouterf, Martin Poncelet, Stéphane Roux, Clément Jailin, Amine Bouterf, Martin Poncelet, and Stéphane Roux. In situ μ CT-scan mechanical tests : Fast 4D mechanical identification. 2017.

[50] Wei-Bin Zhang et al. In-Situ X-ray Tomography Observation of Structure Evolution in 1,3,5-Triamino-2,4,6-Trinitrobenzene Based Polymer Bonded Explosive (TATB-PBX) under Thermo-Mechanical Loading. Materials, pages 1–14, 2018.

[51] Stewart et al. Synthesis and Preclinical Characterization of a Cationic Iodinated Imaging Contrast Agent (CA4+) and Its Use for Quantitative Computed Tomography of Ex Vivo Human Hip Cartilage. 2017.

[52] Keith Wan Kee Ng. Vascular Function and Structure in the Rat Aorta. Cambridge Scholars Publisher, (January), 2013.

[53] R Erbel, F Alfonso, C Boileau, O Dirsch, B Eber, A Haverich, H Rakowski, J Struyven, K Radegran, U Sechtem, J Taylor, Ch Zollikofer, Internal W W Klein, B Mulder, and L A Providencia. Task Force Report Diagnosis and management of aortic dissection. European Heart Journal, (22):1642–1681, 2001.

[54] J. Moini. Phlebotomy: principles and practice. Jones & Bartlett Learning, Burlington, MA, 2013.

[55] T E Clark, M A Lillie, A W Vogl, J M Gosline, and R E Shadwick. Mechanical contribution of lamellar and interlamellar elastin along the mouse aorta. Journal of Biomechanics, 48(13):3599–3605, 2015.

[56] Camilla Go, Joakim Nilsson, Jenny Nordquist, Millvej Kristensson, Kristian Svensson, Charlotte So, Marianne Israelson, and Håkan Garpenstrand. Overexpression of Semicarbazide-Sensitive Amine Oxidase in Smooth Muscle Cells Leads to an Abnormal Structure of the Aortic Elastic Laminas. 163(5):1921–1928, 2003.

[57] B Trachet, P Segers, F Claes, and A Berges. Measuring Mouse Abdominal Aorta Dimensions in Vivo : A Comparison between (3D) Ultrasound and Micro-CT. pages 418–421, 2010.

[58] Bram Trachet, Rodrigo A Fraga-silva, and Francisco J Londono. Performance Comparison of Ultrasound- Based Methods to Assess Aortic Diameter and Stiffness in Normal and Aneurysmal Mice. pages 1–20, 2015.

[59] Jason B. Wheeler, Rupak Mukherjee, Robert E. Stroud, Jeffrey A. Jones, and John S. Ikonomidis. Relation of murine thoracic aortic structural and cellular changes with aging to passive and active mechanical properties. Journal of the American Heart Association, 4(3):e001744, 2015.

[60] Bo Blomgren and Camilla Go. A novel method for quantification of the folding of elastic laminae in elastic arteries. 39:623–630, 2008.

[61] Petra Poliacikova, Adam De Belder, and Mic Clarke. Coronary Stent Implantation Technique: Prolonged Inflation Time Maximizes Stent Expansion. The Journal of invasive cardiology, 2013.

[62] Lloyd W. Klein. Coronary Stenosis Morphology: Analysis and Implication. Springer, Boston, MA, 1997.

[63] Jaryl Ng, Nicolas Foin, Hui Ying, Jiang Ming, Sayan Sen, Sukhjinder Nijjer, Ricardo Petraco, Carlo Di, Justin Davies, and Philip Wong. Over-expansion capacity and stent design model : An update with contemporary DES platforms Over-expansion capacity and stent design model : An update with contemporary DES platforms. International Journal of Cardiology, 221(June):171–179, 2016.

[64] Gerhard A. Holzapfel and Ray W. Ogden. Constitutive modelling of arteries. Proceedings of the Royal Society A: Mathematical, Physical and Engineering Sciences, 466(2118):1551–1597, 2010.

[65] Júlia López-guimet, Jordi Andilla, Pablo Loza-alvarez, and Gustavo Egea. High-Resolution Morphological Approach to Analyse Elastic Laminae Injuries of the Ascending Aorta in a Murine Model of Marfan Syndrome. (April):1–13, 2017.

[66] Wanchoo N et al Saatchi S, Azuma J. Three-dimensional microstructural changes in murine abdominal aortic aneurysms quantified using immunofluorescent array tomography. J Histochem Cytochem, 60:97–109, 2 2012.

[67] *The Gocator 2300 micro-laser scanner*, lmi technologies. `https://lmi3d.com/products/gocator/g2/2300-series/laser-line-profile-sensors` (Accessed April 30th 2020).

[68] *Testing Machines for Cruciform Tests*, zwick/roell. `https://www.zwickroell.com/en/biaxial-testing-machines/cruciform-testing-machine` (Accessed April 28th 2020).

[69] José M Atienza, Francisco J Rojo, Raúl J Burgos, Carlos García-montero, Francisco J Goicolea, Paloma Aragoncillo, and Manuel Elicesa. The Influence of Pressure and Temperature on the Behavior of the Human Aorta and Carotid Arteries. 60(3):259–267, 2007.

[70] *The VIC-2D System*, correlated solutions. `https://www.correlatedsolutions.com/vic-2d/` (Accessed April 28th 2020).

[71] Ogden Ray W Gasser T. Christian and Holzapfel Gerhard A. Hyperelastic modelling of arterial layers with distributed collagen fibre orientations. Journal of the Royal Society Interface, pages 15–35, 2006.

[72] Jos Vander Sloten Nele Famaey Heleen Fehervary, Marija Smoljkic. Planar biaxial testing of soft biological tissue using rakes : A critical analysis of protocol and fitting process. Journal of the mechanical behavior of biomedical materials, 61:135–151, 2016.

[73] Mazur Peter. Freezing of living cells : mechanisms and implications. American Physiological Society, 247(19):0–4, 1984.

[74] Lifeng Lin. Bias caused by sampling error in meta-analysis with small sample sizes. PLOS ONE, 13(9):1–19, 09 2018.

[75] Dominique Tremblay, Tiffany Zigras, Raymond Cartier, Louis Leduc, Jagdish Butany, Rosaire Mongrain, and Richard L. Leask. A comparison of mechanical properties of materials used in aortic arch reconstruction. The Annals of Thoracic Surgery, 88(5):1484 – 1491, 2009.

[76] Henderson SC et al. Ayres C, Bowlin GL. Modulation of anisotropy in electrospun tissue-engineering scaffolds: Analysis of fiber alignment by the fast fourier transform. Biomaterials, 27(32):5524–5534, 06 2006.

[77] Chantal Ayres, Gary L Bowlin, Scott C Henderson, Leander Taylor, Jackie Shultz, John Alexander, Todd A Telemeco, and David G Simpson. scaffolds : Analysis of fiber alignment by the fast Fourier transform. 27(32):5524–5534, 2010.

[78] MS Sacks and CJ Chuong. Characterization of collagen fiber architecture in the canine diaphragmatic central tendon. Journal of biomechanical engineering, 114(2):183—190, May 1992.

[79] Comparative Analysis of Porcine and Human Thoracic Aortic Stiffness. European Journal of Vascular & Endovascular Surgery, 55(4):560–566, 2018.

[80] Claudio M García-Herrera, Diego J Celentano, Marcela A Cruchaga, Francisco J Rojo, José Miguel Atienza, Gustavo V Guinea, and José M Goicolea. Mechanical characterisation of the human thoracic descending aorta: experiments and modelling. Computer methods in biomechanics and biomedical engineering, 15(2):185—193, 2012.

[81] Zhou A Utzinger U Vande Geest J. Haskett D, Johnson G. Microstructural and biomechanical alterations of the human aorta as a function of age and location. Biomech Model Mechanobiol, 12(2):725–736, 2013.

[82] Alice Corbay. Biomechanics - Mechanical characterization of artery tissue and synthetic arterial grafts. Ecole polytechnique de Louvain, Université catholique de Louvain, Prom. : Kerckhofs, Greet ; Lacroix, Valérie., 2019-2020.

[83] Florencia montini ballarin, Daniel Calvo, Pablo Caracciolo, Francisco Rojo, Patricia Frontini, Gustavo Abraham, and Gustavo Guinea-Totuero. Mechanical behavior of bilayered small-diameter nanofibrous structures as biomimetic vascular grafts. Journal of the Mechanical Behavior of Biomedical Materials, 60, 02 2016.

[84] Pourdeyhimi B. et al. A Review of Structural and Material Properties of Vascular Grafts. Journal of Biomaterials Applications, 2(2):163–204, 1987.

[85] Pierce DM Regitnig P Holzapfel GA Schriefl AJ, Zeindlinger G. Determination of the layer-specific distributed collagen fibre orientations in human thoracic and abdominal aortas and common iliac arteries. J R Soc Interface, 71:1275–1286, 9 2012.

[86] Laurie A. Tomlinson and Ian B. Wilkinson. Does it matter where we measure blood pressure? British Journal of Clinical Pharmacology, 74(2):241–245, 2012.

[87] Jos Vander Sloten Heleen Fehervary and Nele Famaey. Development of an improved parameter fitting method for planar biaxial testing using rakes. pages 1–17, 2019.

UNIVERSITÉ CATHOLIQUE DE LOUVAIN
École polytechnique de Louvain
Rue Archimède, 1 bte L6.11.01, 1348 Louvain-la-Neuve, Belgique | **www.uclouvain.be/epl**